International Journal of Remote Sensing
Vol. 29, No. 3, 10 February 2008, 801–829

Phytoplankton size-structure on the western shelf of the Antarctic Peninsula: a remote-sensing approach

M. A. MONTES-HUGO*†, M. VERNET†, R. SMITH‡ and K. CARDER§
†Integrative Oceanography Division, Scripps Institution of Oceanography, University of California, San Diego, 9500 Gilman Drive, CA 92093-0238, USA
‡Department of Geography, Institute for Computational Earth System Science, University of California at Santa Barbara, Santa Barbara, CA 93106, USA
§Department of Marine Science, University of South Florida, 140 7th Avenue South, St. Petersburg, FL 33701, USA

(*Received 9 July 2006; in final form 25 January 2007*)

Remote-sensing models based on total (b_b) and particle (b_{bp}) backscattering are proposed for estimating phytoplankton size-structure characteristics over the Western Antarctic Peninsula (WAP) waters. It is hypothesized that phytoplankton assemblages with larger cells will have lower spectral b_b and b_{bp} slopes (γ). Likewise, a higher concentrations of total chlorophyll *a* (chl_T) will coincide with larger phytoplankton cells. Values of $\gamma_{b_{bp}}$, derived from satellite and *in situ* remote-sensing reflectance (R_{rs}) measurements were matched up with field determinations of chlorophyll *a* concentration fractions ($chl_{(>20\,\mu m)}$ and $chl_{(0.45–20\,\mu m)}$) collected between 1997 and 2006 as part of the Palmer-LTER project. Functionalities between *in situ* measurements of γ_{b_b} and chlorophyll *a* fractions were also investigated. A consistent inverse relationship between $chl_{(>20\,\mu m)}/chl_T$ and γ (b_b and b_{bp}) values was found and verified with two approaches: spatial matchup of satellite monthly composites and time–space matchup of photosynthetic pigment markers. Based on satellite data, a $\gamma_{b_{bp}}$ value of 1.668 was a fair predictor to differentiate WAP waters dominated by 'large' ($chl_{(>20\,\mu m)}/chl_T \geq 0.5$, $\gamma_{b_{bp}} \leq 1.668$) vs 'small' ($chl_{(>20\,\mu m)}/chl_T < 0.5$, $\gamma_{b_{bp}} > 1.668$) phytoplankton cells. A significant negative linear relationship between 19′-butanoyloxyfucoxanthin, fucoxanthin, and $\gamma_{b_{bp}}$ values suggest that *Phaeocystis* aggregates and large diatoms ($>20\,\mu m$) would explain most of the $chl_{(>20\,\mu m)}/chl_T$-γ variability. No relationships were evident between chl_T values and γ values. Although our results cannot be generalized to other oceanic regions, this work is the first to provide evidence about the significant influence of phytoplankton size distributions on spectral backscattering of WAP waters. Furthermore, and based on chlorophyll *a* fraction analysis, it was the $>20\,\mu m$ phytoplankton cells that were responsible for such γ variations seen on satellite and *in situ* values.

*Corresponding author. Email: mmontes@coast.ucsd.edu

International Journal of Remote Sensing
ISSN 0143-1161 print/ISSN 1366-5901 online
http://www.tandf.co.uk/journals
DOI: 10.1080/01431160701297615

1. Introduction

Phytoplankton size-structure plays a crucial role in controlling the trophic and biogeochemical functioning of pelagic ecosystems (Tremblay and Legendre 1994). The relative proportion between cells with different size is a decisive factor for selecting food transference pathways (phytoplankton–zooplankton vs phytoplankton–bacteria), carbon export into deep waters, nutrient cycling in the euphotic zone and differential sequestering of atmospheric CO_2 (Walsh *et al.* 2001). Consequently, characterization of phytoplankton size distributions provides crucial information for modelling global climate change scenarios. For instance, in the Southern Ocean, alterations of phytoplankton size distributions have been related to reduced surface water salinities caused by a regional warming trend (Moline *et al.* 2004a).

Mesoscale mapping of the phytoplankton size-structure using traditional (e.g. microscopic observations; Garibotti *et al.* 2003b) or advanced (e.g. flow cytometer; Collier 2000) oceanographic methods is generally arduous or deals with relatively expensive instruments that require a high degree of technical expertise. Furthermore, ship surveys are costly and time-consuming, and do not allow a complete and simultaneous coverage of the study area. Fortunately, the use of space-borne remote-sensing measurements may overcome these field-sampling limitations. Indirect estimation of the phytoplankton size-structure has been proposed using bio-optical algorithms based on light absorption (e.g. influence of cell size on packaging effect; Carder *et al.* 1986, Ciotti *et al.* 1999). However, no ocean-colour relationships exist to link satellite remote-sensing reflectance (R_{rs}) with phytoplankton size-structure using a 'direct' approach.

Similar to absorption coefficients ($a=c-b$, where c and b are the total attenuation and scattering coefficients, respectively; table 1), total backscattering coefficients (b_b) at different wavelengths can be obtained in a reliable way from inversion of R_{rs} spectra (Weidemann *et al.* 1995, Carder *et al.* 1999a, Moline *et al.* 2004b). Notice that b_b values have two contributions: water or molecular (b_{bw}) and particles (b_{bp}). Interpretation of spectral shapes of particle backscattering (b_{bp}) is a widespread tool to derive bulk particle size characteristics of field samples (Gordon and Morel 1983, Green and Sosik 2004, Aas *et al.* 2005). As the size of the particles decreases and/or monodispersion is approached (e.g. phytoplankton bloom), a larger variability of b_b and b_{bp} spectral shapes is observed (Gordon and Morel 1983, Vaillancourt *et al.* 2004). A general spectral model of backscattering is:

$$b_{bx}(\lambda) = M(\lambda_o/\lambda)^{\gamma_{b_{bx}}}, \quad (1)$$

where λ is the light wavelength in the visible range (400–700 nm), x indicates the total (water + particles) or particle components, M is the magnitude of backscattering at the reference wavelength λ_o, and $\gamma_{b_{bx}}$ is the spectral slope that increases as particles become smaller, or when the water contribution is larger. The parameter M is generally a function of b_b (555) (Reynolds *et al.* 2001), b_{bp} (400) (Lee *et al.* 1999), b_{bp} (555) (Lee *et al.* 2002), or R_{rs} (555) (Carder *et al.* 1999b), while $\gamma_{b_{bx}}$ can be assumed constant (Morel 1973) or variable (Lee *et al.* 1996, Carder *et al.* 1999b, Reynolds *et al.* 2001). Based on lab experiments, field measurements, and Mie theory calculations, there is no general consensus as to whether the spectral shape of b_{bp} is controlled by phytoplankton (Bricaud and Morel 1986, Vaillancourt *et al.* 2004), aggregates (Flory *et al.* 2004), colloids (Stramski and Wozniak 2005), or non-living particles (detritus and minerals; Stramski *et al.* 2001). Most of this

Table 1. Summary of main acronyms and notation.

Abbreviation	Definition	Units
WAP	Western Antarctic Peninsula	
PRR	profiling reflectance radiometer	
Pal-LTER	Palmer-Long Term Ecological Research project	
MLAC	merged local area coverage	
GAC	global area coverage	
HPLC	high-pressure liquid chromatography	
SMMR	scanning multi-channel microwave radiometer	
SSM/I	special sensor microwave/imager	
RMSlog	root mean square error of $\log_{10}$ values	
ε_{rr}	linear error	
$\varepsilon_{Filter(>20\mu m)}$	detection error of waters dominated by $>20\,\mu m$ phytoplankton cells	
ρ	sea-surface reflectance	
t_d	transmittance across the sea-surface	
n_w	index of refraction of water	
R_{rs}	remote-sensing reflectance	sr^{-1}
nL_w	normalized water leaving radiance	$W\,m^{-2}\,sr^{-1}\,nm^{-1}$
F_o	extraterrestrial solar irradiance	$W\,m^{-2}$
E_d	downwelling irradiances	$W\,m^{-2}$
L_u	upwelling radiance	$W\,m^{-2}\,sr^{-1}\,nm^{-1}$
K_d	vertical downwelling diffuse attenuation coefficient	m^{-1}
K_d*	chlorophyll *a*-normalized K_d	$m^2\,mg\,chl^{-1}$
β_{140}	volume scattering function measured at 140°	$sr^{-1}\,m^{-1}$
χ	conversion factor of backscattering meter	sr
σ	sigma correction factor of backscattering	
b	scattering coefficient	m^{-1}
c	attenuation coefficient	m^{-1}
b_b	total backscattering coefficient	m^{-1}
b_b'	uncorrected total backscattering coefficient	m^{-1}
b_{bp}	particle backscattering coefficient	m^{-1}
b_{bw}	water backscattering coefficient	m^{-1}
$\overline{b_b}$	backscattering efficiency	
γ	spectral backscattering slope	
a	absorption coefficient	m^{-1}
a_w	water absorption coefficient	m^{-1}
a_g	gelbstoff absorption coefficient	m^{-1}
a_d	detritus absorption coefficient	m^{-1}
a_{ph}*	chlorophyll *a*-normalized phytoplankton absorption coefficient	$m^2\,mg\,chl^{-1}$
ξ_g	slope of gelbstoff spectral absorption	λ^{-1}
ξ_d	slope of detritus spectral absorption	λ^{-1}
chl_T	total chlorophyll *a* concentration	$mg\,m^{-3}$
chl_{DS}	chlorophyll *a* concentration at the surface estimated by Dierssen and Smith (2000) algorithm	$mg\,m^{-3}$
chl_{b_b}	total chlorophyll *a* concentration averaged between 0 and 10 m	$mg\,m^{-3}$
$\overline{Q_{b_b}}$	spectral backscattering efficiency	

discrepancy assessing the role of each backscatter component to spectral b_{bp} values is related to the lack of *in situ* and satellite measurements and uncertainties of scattering phytoplankton models (Quirantes and Bernard 2004). We hypothesize that phytoplankton assemblages with a different mean bulk cell size will have different spectral backscattering signatures (e.g. phytoplankton communities with larger cells will have lower spectral b_b and b_{bp} slope values).

The aim of this study is to examine the bio-optical relationships between slopes (γ_{b_b} and $\gamma_{b_{bp}}$) of spectral backscattering coefficients (b_b and b_{bp}), and size-structure parameters of oceanic and coastal marine phytoplankton communities of the Southern Ocean. Size-backscattering functionalities were tested with phytoplankton samples obtained during the Palmer Long-Term Ecological Research project (Pal-LTER) in the western shelf of the Antarctic Peninsula (WAP). The Pal-LTER programme has been active since 1993 as a sustained framework to elucidate physical and biological mechanisms affecting the Antarctic ecosystem including phytoplankton dynamics along a large time–space range of scales (Smith *et al.* 1995). Remote-sensing empirical relationships based on spectral slope of b_{bp} values will be investigated using chlorophyll *a* fractions, *in situ* R_{rs} estimations, and satellite R_{rs} data from the Sea-viewing Wide Field-of-view Sensor (SeaWiFS) collected during summer cruises. Likewise, since the total phytoplankton chlorophyll *a* concentration (chl_T) and cell abundance correlate inversely with mean cell size over the WAP area (Bidigare *et al.* 1996), the relationships between chl_T and phytoplankton size-structure will also be explored.

2. Methods

2.1 *Size-structure indices*

To estimate the average bulk cell size of diverse phytoplankton assemblages of WAP waters, two size-structure indices were analysed: $\gamma_{b_{bx}}$ and chl_T. Since both parameters can be estimated from R_{rs} measurements, they can be used to map horizontal distributions of phytoplankton size spectra, even from space.

2.1.1 Spectral slope of particle and total backscattering coefficient. The spectral slope of particle backscattering coefficient ($\gamma_{b_{bp}}$) is an optical parameter that is sensitive to variations of particle size distributions and water/particle contributions (Gordon *et al.* 1980, Gordon and Morel 1983). In Antarctic waters not influenced by terrigeneous inputs, phytoplankton is the main optical constituent affecting particle light attenuation, since detritus is normally in low concentrations (Mitchell and Holm-Hansen 1991, Dierssen *et al.* 2002). Hence, in Southern Ocean waters, it might be expected that variability on $\gamma_{b_{bx}}$ is connected to modifications of phytoplankton size-structure.

Values of $\gamma_{b_{bp}}$ were obtained using an empirical relationship proposed originally for the Moderate Resolution Imaging Spectroradiometer (MODIS) and adjusted with data collected over upwelling regions and high-latitude waters of Antarctica including the WAP survey site (Carder *et al.* 2004):

$$\gamma_{b_{bp}} = Y_0 + Y_1 R_{rs}(443)/R_{rs}(488)\, Y_0 = -1.13,\ Y_1 = 2.57. \tag{2}$$

Original MODIS wavelengths are slightly different from SeaWiFS wavelengths (e.g. 488 nm instead of 490 nm), even though these differences (~2 nm) may be considered negligible (O'Reilly *et al.* 1998). Computation of $\gamma_{b_{bp}}$ is part of a semi-empirical model of chl_T and absorption that accounts for phytoplankton acclimation (i.e. packaging effect or flattening of phytoplankton absorption peak with increasing intracellular pigment concentration) to different light and nutrient regimes (Carder *et al.* 1999b). Values of $\gamma_{b_{bp}}$ (slope in equation (1)) are estimated by inversion of R_{rs} with a predictor-corrector approach (Lee *et al.* 1994). Notice that parameterization of Y_0 and Y_1 is relatively insensitive to phytoplankton

photoacclimation (Carder *et al.* 2004). Since gelbstoff, detritus, and phytoplankton absorption values covary in Antarctic waters (Reynolds *et al.* 2001), the reflectance ratio in equation (2) is mainly influenced by spectral changes in backscattering.

Due to the dependence between b_{bp} and b_b, it would not be surprising to expect analogous relationships between changes on γ_{b_b} and phytoplankton size-structure characteristics. Based on field measurements, Reynolds *et al.* (2001) found an inverse relationship between γ_{b_b} and b_b (555) values of Ross Sea and Antarctic Polar Front samples:

$$\gamma_{b_b} = -3.616 \log_{10}[b_b(555)] - 6.866. \quad (3)$$

Unlike equation (2), equation (3) may not be computed with satellite R_{rs} measurements over the WAP region for two reasons: (1) the γ_{b_b} algorithm was developed with data collected over waters with a phytoplankton community and optical environment different from that typical of the western shelf of the Antarctic Peninsula; (2) the resulting model is inaccurate due to two additive errors, one related to b_b (555) estimation and the other linked to γ_{b_b} calculation. Despite these limitations, *in situ* γ_{b_b} estimations were made to further support potential relationships between spectral backscattering curves and size properties of phytoplankton samples (see *in situ* optical measurements).

2.1.2 Total chlorophyll *a*. Although the use of chl_T to infer phytoplankton cell size gradients in Antarctic waters was pointed out during the 1990s (Smetacek *et al.* 1990, Bidigare *et al.* 1996), *in situ* and remote-sensing chl_T measurements made over the WAP waters have been uniquely applied to study spatial and temporal changes on phytoplankton primary production or biomass. In this study, a regional R_{rs} algorithm proposed for WAP waters will be used to derive chl_T (hereafter chl_{DS}; Dierssen and Smith 2000):

$$chl_{DS} = 10^{A + BX + CX^2 + DX^3}, \quad (4)$$

where $X = \log(R_{rs}(490)/R_{rs}(555))$, $A = 0.641$, $B = -2.058$, $C = -0.442$, and $D = -1.140$.

The reflectance model in equation (4) was developed with a large bio-optical data set (>1000 stations) and differs from other models proposed for estimating chl_T in lower-latitude oceanic regions around the world. Over the WAP region, water-leaving radiance is significantly higher in the blue region and lower in the green region of the spectrum for chl_T values $>1\,mg\,m^{-3}$ (Dierssen and Smith 2000). For this reason, the chl_{DS} values are roughly twice as high as those chl_T calculated from global ocean colour models such as SeaWiFS OC-4 (O'Reilly *et al.* 1998).

2.2 *Optical measurements*

2.2.1 *In situ*. A field survey of optical properties consisted of two datasets, one dedicated to estimate $\gamma_{b_{bp}}$ using apparent radiometric quantities (e.g. R_{rs}) and the other designed to derive γ_{b_b} from single-angle volume scattering function measurements at different wavelengths and lab determinations of inherent optical quantities (e.g. particle and gelbstoff absorption).

In the first approach, optical properties were estimated (R_{rs}) or measured (E_d: downwelling irradiance and L_u: upwelling radiance) with a profiling reflectance radiometer (PRR, Biospherical Instruments Inc.) between 1998 and 2006. The multiyear dataset was composed of profiles collected in waters with different levels

of chl_T and distances to the shore. Due to the loss of PRR-600/610 during a storm, optical measurements after 2002 were performed with a PRR-800/810. Both instruments share the same radiometric channels (412, 443, 490, 510, 555, and 665 nm), but PRR-800/810 has two additional spectral bands in the visible range (532 and 670 nm). The sampling grid (500 km along the shelf × 250 km across the shelf) was covered in 6 weeks during January/February of each year (figure 1). PRR profiles were performed between 6:00 and 17:00 h from the Sun-illuminated side of the ship. Correction of E_d and L_u values by depth and dark count offsets was performed for each profile following Smith *et al.* (1997). Calculations of E_d and L_u values just below the sea surface were obtained by linear regression of values in a semi-log scale within 0–5 m (inshore) and 0–15 m (middle-shelf and oceanic waters), and extrapolation of the fitting curve to the surface. Notice that vertical

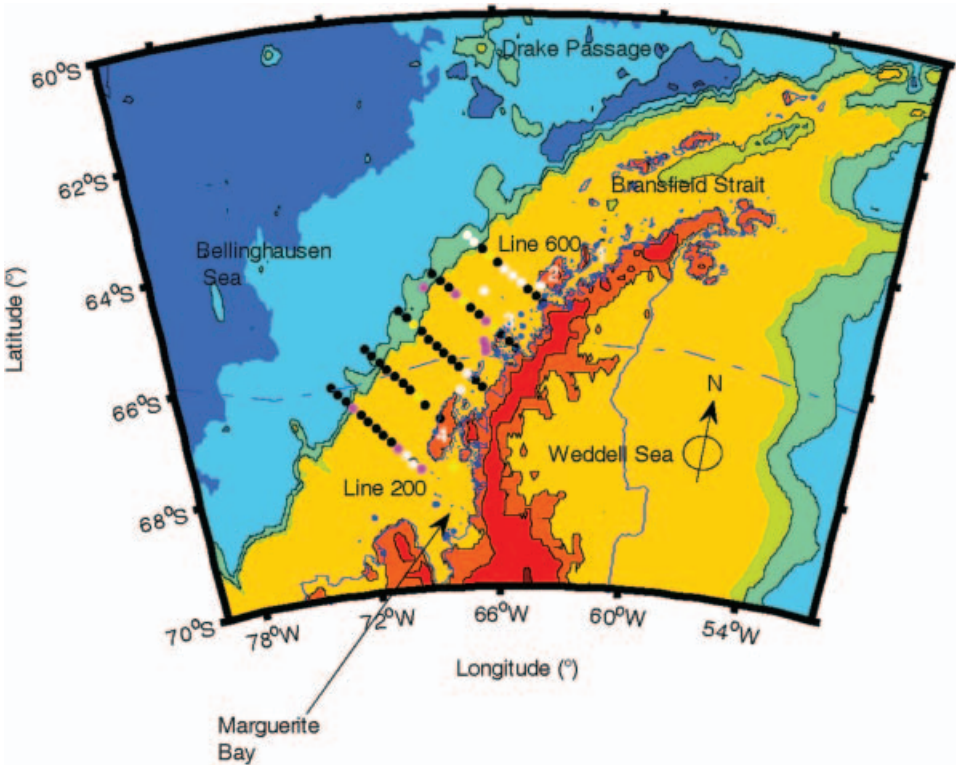

Figure 1. Map of the study area. Geographic points are represented using a conic Lambert projection. Sampling grid stations of Palmer LTER region (•). 1: Bransfield Strait; 2: Anvers Island; 3: Renaud Island; 4: Adelaide Island. Shelf lines 200–600 are spaced every 100 km and are covered during each cruise in about 28 days. Across-shelf stations 0–60, 80–120, and 140–220 contain inshore, middle shelf, and shelf-break or slope stations. Medium-resolution coastline data (1 : 75 000) were obtained from the NOAA/NOS coastline extractor website and include the perennial sea ice edge (http://rimmer.ngdc.noaa.gov/mgg/coast/getcoast.html) (continuous blue line). The seasonal sea ice extent is indicated for an average year (summer 1997) (National Snow and Ice Data Center is shown; Smith and Stammerjohn 2001) (dashed blue line). Bathymetric contours were constructed with a 5-min (~8 km) topographic dataset with isobaths every 1 km (TerrainBase, National Geophysical Data Center). Match-ups between PRR (white circles), HPLC (magenta circles), HydroScat-6 (yellow circles), and $chl_{(>20\,\mu m)}$ data (all circles) are shown as solid circles.

downwelling diffuse attenuation coefficient (K_d) values can be derived from slope values of E_d regressions (Smith and Baker 1981). To avoid spectral artifacts (e.g. due to variable cloud cover) on E_d and L_u, only those profiles made during clear days and ice-free conditions were chosen. R_{rs} below the sea-surface was derived from $L_u(0^-, \lambda)$ and $E_d(0^-, \lambda)$:

$$R_{rs}(0^-, \lambda) = L_u(0^-, \lambda)/E_d(0^-, \lambda). \quad (5)$$

A posteriori, $R_{rs}(0^-, \lambda)$ was scaled by a transmission factor (t_r) to obtain R_{rs} above the sea surface or $R_{rs}(0^+, \lambda)$:

$$R_{rs}(0^+, \lambda) = t_r(\lambda) R_{rs}(0^-, \lambda) \quad (6)$$

$$t_r(\lambda) = t_d(1-\rho(\lambda,\theta))/n_w^2. \quad (7)$$

A water–air Fresnel reflectance ($\rho(\lambda, \theta)$) of 0.021–0.022 was assumed and spectrally corrected (Mobley 1994), n_w is the index of refraction of water at 0°C and the transmittance across the sea surface (t_d) was approximated to 0.96 (Smith and Baker 1986). Similar to theoretical findings (Mobley 1994), t_r values varied between 0.515 and 0.524. The consistency of $R_{rs}(0^+, \lambda)$ estimations was checked using surface radiometric measurements. Although no direct *in situ* measurements of $R_{rs}(0^+, \lambda)$ were performed to validate PRR estimates, a maximum of 24% error (root mean square) based on field sampling conditions (Toole *et al.* 2000) is expected. PRR-derived $R_{rs}(0^+, \lambda)$ values were used to calculate $\gamma_{b_{bp}}$ according to Carder *et al.* (2004).

In the second approach, spectral backscattering measurements at one angle were made between 10 and 25 January 2001 (figure 1) using a backscattering meter (HydroScat-6 or HS-6, Hobi Labs). For each channel (442, 488, 532, 555, 620, and 676 nm), readings within each of the first 10 m were binned and averaged after correcting each profile by path-length attenuation (sigma factor). Uncorrected total backscattering coefficients ($b_b(\lambda)'$) were estimated from the uncorrected volume scattering function measured at 140° (β_{140u}):

$$b_b(\lambda)' = b_{bw}(\lambda) + 2\pi\chi[\beta_{140u}(\lambda) - \beta_{140w}(\lambda)] \text{(Dana and Maffione 2002)} \quad (8)$$

$$\beta_{140w}(\lambda) = \beta_{140w}(\lambda_o)[(\lambda_o)/\lambda]^{4.32} \text{(Morel 1974)}. \quad (9)$$

The contribution of water to backscattering (b_{bw}) is $0.5b_w$, where b_w is derived for the clearest oceanic measurements (salinity=35; Morel 1974, Smith and Baker 1981), χ=1.08 sr is a conversion factor that varies slightly and linearly around 120°, and depends on sensor geometry (Oishi 1990), β_{140w} is the uncorrected water backscattering contribution, and λ_o is a reference wavelength (Hobi Labs uses 525 nm). Corrected spectral backscattering values were obtained after correction of scattered signal by two methods: light source-sample volume and sample volume-detector; and path-length attenuation or sigma factor (σ):

$$b_b(\lambda) = \sigma b_b(\lambda)' \text{(Dana and Maffione 2002)} \quad (10)$$

$$\sigma = k_1 e^{k_{exp} k_{b_b}} \quad (11)$$

$$\begin{aligned} K_{bb}(\lambda) &= a(\lambda) + 0.4b(\lambda) \\ &= a_w(\lambda) + 0.06a_{ph}^*(\lambda)\text{chl}_T^{0.65} \\ &\quad 1 + 0.2e^{-\xi \cdot g(\lambda_r - 440)} + a_d(400)e^{-\xi \cdot d(\lambda_r - 440)} + 0.4\left(b_b(\lambda)' - b_{bw}(\lambda)\right)\Big/\overline{b_b}.. \end{aligned} \quad (12)$$

k_1 is a calibration parameter that compensates for the attenuation in the water used for the calibration (~1), K_{b_b} accounts for the optical medium attenuation, K_{exp} is a calibration parameter which is specific to the individual instruments. Notice that in equation (12) the absorption term is a variant of Morel's (1991) model where there is implicitly a covariation between phytoplankton and gelbstoff absorption of light. Originally, the a and b coefficients are derived from a spectral beam attenuation instrument (AC-9, WetLabs). In this work, values of chlorophyll-specific phytoplankton (a_{ph}*), detritus (a_d), and gelbstoff (a_g) absorption, and spectral slopes of gelbstoff (ξ_g) and detritus (ξ_d) were obtained from spectrophotometric measurements (Perkin-Elmer Lambda 40) of water samples (Fargion and Mueller 2000) gathered between 0 and 8 m. Similar to other studies in Antarctic waters (Reynolds *et al.* 2001), reliable gelbstoff determinations were done with a 10-cm quartz cuvette (signal-to-noise=3–5). Water absorption (a_w) between 400 and 700 nm is derived for pure water samples (Pope and Fry 1997) and adjusted by temperature and salinity changes (Pegau and Zanaveld 1993, Pegau *et al.* 1997). Values of ξ_g were calculated by fitting a single exponential model to spectral curves of gelbstoff absorption:

$$a_g(\lambda) = a_g(\lambda_r)e^{-\xi_g(\lambda_r - \lambda)} \quad \text{(Jerlov 1976)}. \tag{13}$$

Unlike hyperbolic models, the exponential adjustment is highly affected by the spectral range, even though it is the most used model for remote-sensing algorithms (Twardowski *et al.* 2004). To match equation (12), λ_r was 440 nm instead of 412 nm, the reference wavelength used by Jerlov (1976). Nonlinear regression using the Marquardt–Levenberg algorithm was used between 412 and 590 nm, since this range is important for ocean colour relationships and is not influenced by absorption of other dissolved compounds such as salts. Preliminary results showed insignificant differences between hyperbolic and exponential models to estimate ξ_g between 412 and 590 nm. Values of ξ_d were also computed between 412 and 590 nm using equation (13) and λ_r of 400 nm.

Backscattering efficiency ($\overline{b_b} = b_b/b$) was estimated from Monte Carlo simulations for waters with chl_T values of 0.3 ($\overline{b_b} = 0.025272$) and 5 mg m^{-3} ($\overline{b_b} = 0.018127$) (Montes-Hugo 2005). Calculation of b_b using equation (10) has a standard error of 9% when values are computed for pure waters (Dana and Maffione 2002). Backscattering error due to temperature changes is compensated by HydroScat-6 using a reference LED. Based on Morel (1974) and Boss and Pegau (2001), error estimation of b_b due to salinity effects (33–35 psu over WAP waters) was considered minor (1.3%) compared with other uncertainties. Spectral slopes of b_b were computed from equation (1) by fitting a log–log curve with a $\lambda_o = 555$ nm and $M = b_b$ (555). Derivation of $\gamma_{b_{bp}}$ from γ_{b_b} after subtracting water backscattering contribution is not recommended on high-nutrient low-chlorophyll a (most chl_T values ~0.1 mg m^{-3}) Antarctic oceanic waters, since seawater accounts for the greatest contribution to $b_b(\lambda)$ at shorter wavelengths of the visible range (Reynolds *et al.* 2001).

2.2.2 Satellite imagery. Merged local area coverage satellite scenes (MLAC) were obtained from SeaWiFS's (http://oceancolour.gsfc.nasa.gov/, NASA). MLAC's have pixels with 1.1-km resolution at nadir and are composite images of several data streams (onboard and HRPT stations) over the region of interest and for a given orbit. For the years 2005 and 2006, only global area coverage images (GAC) with

4.5-km spatial resolution were available. Geolocated and atmospheric corrected imagery products (L2) were collected between 60° S 80° W and 70° S 50° W, so satellite scenes included coastal and oceanic domains of the WAP (figure 1). Furthermore, they encompassed regions where phytoplankton assemblages have a different composition and size-structure (Garibotti *et al.* 2005). Spring and summer images were browsed between 1997 and 2006, and only those swaths containing a minimum of 25% pixels with geophysical units were chosen. To remove multiple-scattering effects (Sun zenith angle greater than 50°) on atmospheric correction (Gordon *et al.* 1988), only image datasets between 1 November and 8 February of each year were analysed. Imagery corresponded to scenes captured between 8:00 and 17:00 local time. For each pixel and wavelength (λ=443, 490, 555 nm) remote-sensing reflectance measurements were derived from normalized water leaving radiance (nL_w) (i.e. the radiance that would exit the ocean in the absence of the atmosphere if the Sun were at the zenith):

$$R_{rs}(\lambda) = nL_w/F_o(\lambda), \tag{14}$$

where $F_o(\lambda)$ is the extraterrestrial solar irradiance (Neckel and Labs 1984).

The Windows Image Manager (WIM) and the Automation module (WAM) software (http://www.wimsoft.com/) was used to read the R_{rs} values from L2 imagery (HDF format). Low-quality pixels were removed from L2 datasets using NASA level 2 flags (appendix at http://iod.ucsd.edu/~mmontes/publications/2006/ International Journal of Remote Sensing). R_{rs}-derived products (e.g. chl_{DS} and $\gamma_{b_{bp}}$) were computed with customized software written within Visual Studio environment in C# and using object classes from Microsoft NET framework.

2.3 *Algorithm validation*

Validation of satellite-derived size-structure indices was carried out with *in situ* samples of chlorophyll *a* fractions ($chl_{(>20\,\mu m)}$ and $chl_{(0.45–20\,\mu m)}$) collected between November 1997 and March 2006 over the WAP region by the Pal-LTER project. Regarding the Pal-LTER database size (>29 000 data), a program written in Matlab (version 7.1) was used to calculate the chlorophyll *a* fractions for each cruise. In general, chlorophyll *a* fractions were obtained at the 50% light level and within the first optical depth or $1/K_d$ (~1.9–21 m when λ is 490 nm; ~90% of water-leaving radiance is originated within that layer; Gordon and McCluney 1975).

Samples of chl_T, $chl_{(>20\,\mu m)}$ and $chl_{(0.45–20\,\mu m)}$ were analysed fluorometrically (Smith *et al.* 1981). The percentages of $chl_{(>20\,\mu m)}$ and $chl_{(0.45–20\,\mu m)}$ were calculated with respect to the non-fractioned chlorophyll *a* sample of the same light level depth. Each chlorophyll *a* fraction was normalized by the sum of both fractions in each station, and when $chl_{(0.45–20\,\mu m)}$ was not available, the smaller chlorophyll fraction was computed by subtracting $chl_{(>20\,\mu m)}$ from chl_T.

Matching between field measurements of chl_T, $chl_{(>20\,\mu m)}$, and $chl_{(0.45–20\,\mu m)}$ and satellite remote-sensing indices of phytoplankton size-structure was performed in batch mode using a WAM matching routine. For each run, the maximum time difference between each ship survey and satellite pass was 4 h. Match-ups of near-shore pixels were eliminated due to the significant radiance contribution of sea-ice. Average and median values for each match-up were computed with a mask of 3-by-3 (MLAC) or 2-by-2 (GAC) pixels. The performance of phytoplankton size-structure indices was tested in two ways. In the first approach, monthly composites (mean of valid pixels, zero does not account) of indices were generated for each year and

classified using a binary mask to indicate those waters with dominance of 'large' (>20 μm) cells (e.g. size index threshold where $chl_{(>20\,\mu m)}$ contribution represents half or more of chl_T). Notice that this threshold was derived from $\gamma_{b_{bp}}$–chlorophyll *a* fractions and chl_T-chlorophyll *a* fractions empirical relationships with a minimum time–space difference between satellite and *in situ* points. *A posteriori* and for each month, field samples of chlorophyll *a* fractions were grouped in sub-regions (inshore, middle shelf and shelf-break or slope; see figure 1) along two sampling lines (600 and 200), and the statistics (median and variance) for each group was calculated.

The same procedure was applied to classified satellite-derived size indices using 5-by-5 (LAC) or 3-by-3 (GAC) pixels. True detected points of $\gamma_{b_{bp}}$ and chl_T indices were those samples where $chl_{(>20\,\mu m)}/chl_T \geqslant 0.5$ and were geolocated inside the sub-region of 'large' particle size distribution (dominance of phytoplankton >20 μm) or high chl_T values ($>4\,mg\,m^{-3}$). Conversely, false detected points were those samples where $chl_{(>20\,\mu m)}/chl_T$ was smaller than 0.5 (dominance of phytoplankton $\leqslant 20\,\mu m$) and fell inside a sub-region of 'small' particle size distribution (dominance of phytoplankton <20 μm) or low chl_T values ($\leqslant 4\,mg\,m^{-3}$). The prediction error of the phytoplankton size-structure mask was computed as:

$$\varepsilon_{\mathrm{Filter}(>20\,\mu m)}(\%) = (1 - \text{True hits}/(\text{True} + \text{False hits}))100. \tag{15}$$

In the second approach, a time–space match-up similar to that proposed for chlorophyll *a* fractions vs phytoplankton size-structure indices was made for the main phytoplankton pigment signatures over the WAP. Since different phytoplankton classes have specific size cell ranges, the relative proportion of each taxonomic group with respect to total chl_T may be used as an estimator of phytoplankton size-structure (Vidussi *et al.* 2001, Bricaud *et al.* 2004). Pigment markers of chlorophytes (chlorophyll *b*), cryptophytes (alloxanthin), dinophytes (peridinin), diatoms (fucoxanthin), prymnesiophytes (19′-hexanoyloxyfucoxanthin and 19′-butonoyloxyfucoxanthin or 19′-BF) were obtained from the Pal-LTER database between 1998 and 2003. These summer samples were originally analysed by high-pressure liquid chromatography (HPLC) according to Garibotti *et al.* (2003a).

2.4 *Statistical analysis*

Accuracy of phytoplankton size-structure indices for estimating chlorophyll *a* fractions was evaluated using the root mean square error in $\log_{10}$ scale (RMS log) of quantity between *N* derived and true chlorophyll *a* fraction (*X*) values (O'Reilly *et al.* 1998):

$$\mathrm{RMS\ log} = \left\{ \sum_{i=1}^{i=n} \left[\log_{10}\left(X_i^{\mathrm{derived}}\right) - \log_{10}\left(X_i^{\mathrm{true}}\right) \right]^2 \Big/ N \right\}^{0.5}. \tag{16}$$

The difference between derived and true *X* values in linear scale is calculated as:

$$\varepsilon_{rr} = 0.5\left[\left(10^{\mathrm{RMS\,log}} - 1\right) + \left(1 - 10^{-\mathrm{RMS\,log}}\right)\right]. \tag{17}$$

These same statistical calculations were applied to backscattering-pigment markers relationships to find out the phytoplankton classes more related to changes

in spectral shape of backscattering coefficients. To estimate the proportion of variation explained by the remote-sensing models, the coefficient of determination (R^2) was calculated using minimization routines (Matlab 7.1).

3. Results

3.1 *Bio-optical indices of phytoplankton size-structure*

3.1.1 Spectral slope of particle and total backscattering coefficient. To gain an insight into the mechanistic effect of diverse phytoplankton cell size spectra on $\gamma_{b_{bx}}$ variability, it is fundamental to figure out first the effect on those optical variables (e.g. R_{rs}) influencing most $\gamma_{b_{bx}}$ behaviour.

The influence of two extreme cases of phytoplankton cell size distributions on $R_{rs}(\lambda)$, an indispensable optical property to derive $\gamma_{b_{bp}}$, is analysed in figure 2(*a*). Remote-sensing reflectance spectra showed two evident features within the blue-green spectral range: a lower R_{rs} slope between 443 and 490 nm for that profile with a smaller phytoplankton size-structure (dominance of cells $<20\,\mu m$) and a reflectance peak circa 555 nm for the larger phytoplankton case (dominance of cells $>20\,\mu m$). The 'large' case is an inshore station of line 400 taken on 2 February 2006 ($chl_T=17.02\,mg\,m^{-3}$, $chl_{(>20\,\mu m)}/chl_T=0.86$) while the 'small' case is a middle

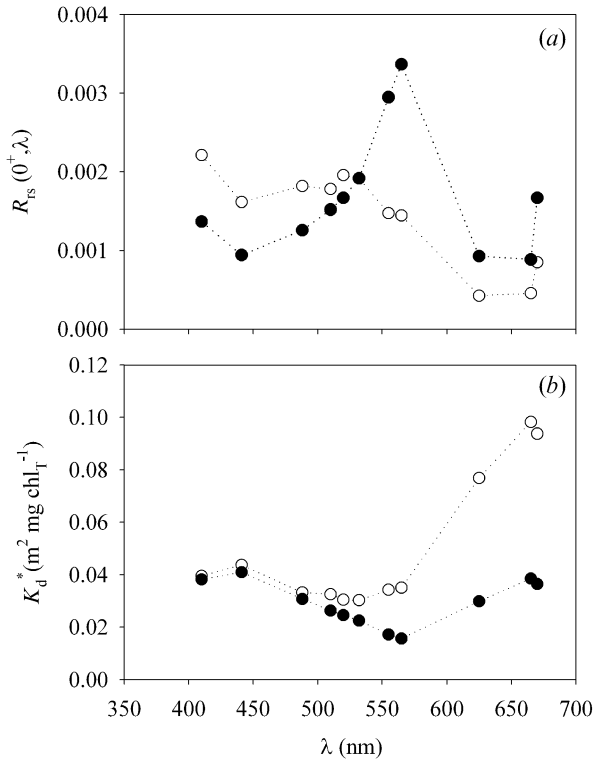

Figure 2. Optical measurements of profiling reflectance radiometer (PRR) in waters with different phytoplankton size-structure; 'large cells' ($[chl_{(>20\,\mu m)}/chl_T]\geq 0.5$, solid circles), 'small cells' ($[chl_{(>20\,\mu m)}/chl_T]<0.5$, empty circles), (*a*) remote-sensing reflectance (R_{rs}), (*b*) K_d chlorophyll *a*-normalized (K_d*). Notice that each curve corresponds to one cast.

shelf station of line 500 obtained on 6 January 2006 ($chl_T = 5.43\ mg\ m^{-3}$, $chl_{(>20\,\mu m)}/chl_T = 0.01$) (figure 1).

As described in §1, the effect of waters with a different phytoplankton size-structure may also have an effect on absorption properties of phytoplankton and, consequently, R_{rs} spectra. K_d is expected to be more affected by changes on light absorption with respect to those changes on light scattering. Therefore, and using the same PRR profiles of figure 2(*a*), spectral shapes of chl_T-normalized $K_d(K_d^*)$ were plotted as a function of two phytoplankton communities with a different size-structure (figure 2(*b*)). Similar to R_{rs}, curve normalization allows biomass-independent effects to be analysed. In general, it seemed that changes on light absorption posed by a different phytoplankton size-structure were weak with respect to those observed with R_{rs} spectra. In both cases, K_d^* values have a medium around 440 nm, a minimum around 550 nm, and an abrupt increase above 550 nm. The first and second spectral features correspond to maximum and minimum phytoplankton absorption peaks due to chlorophyll *a*, while the last feature is consistent with the significant water absorption at longer wavelengths. Greater differences toward the red range were an artifact of K_d normalization (chlorophyll *a* and K_d at 490 nm values were more than three and 100 times lower in the 'small' than in the 'large' phytoplankton case profile).

Figure 3 shows that both PRR-derived and satellite-derived $\gamma_{b_{bp}}$ values generally tended to decrease as the contribution of 'large' phytoplankton cells (>20 μm) became greater. In both curves, only significant semi-log relationships were found when $chl_{(>20\,\mu m)}/chl_T$ data were compared (table 2). Unlike PRR-derived $\gamma_{b_{bp}}$ values (figure 3(*a*)), satellite-derived $\gamma_{b_{bp}}$ estimates had a tighter relationship with $chl_{(>20\,\mu m)}/chl_T$ field measurements due to a lower residual variability (~20%) (figure 3(*b*)). Based on satellite data, the $\gamma_{b_{bp}}$ threshold at which $chl_{(>20\,\mu m)}/chl_T = 0.5$ was 1.668 (figure 3(*b*)). Further examination of statistical results revealed that the intercept of the $\log - [chl_{(>20\,\mu m)}/chl_T] - \gamma_{b_{bp}}$ relationship did not change between field and satellite observations. However, the regression slope was significantly steeper for the PRR with respect to the SeaWiFS curve (table 2).

In order to confirm these satellite and PRR inverse functionalities between $chl_{(>20\,\mu m)}/chl_T$ and $\gamma_{b_{bp}}$ values, simultaneous measurements of *in situ* spectral b_b (water + particles), previously corrected by path-length attenuation, and $chl_{(>20\,\mu m)}/chl_T$ values were compared (table 3). Range of optical properties in table 3 was representative of stations located in inshore and slope waters. Similar to PRR measurements, HydroScat-6 determinations under the influence of coastal effects (e.g. terrigenous detritus) were not considered part of the analysis. Blue-green absorption was driven mainly by phytoplankton ($a_{ph}(440)/a_g(440)$ values between 19.8 and 188.7). A relatively large range in phytoplankton and gelbstoff absorption values (>30%) had little influence on $\sigma(555)$ variability (<1%) even when shorter (greater absorption due to gelbstoff and phytoplankton) and longer (greater absorption due to water) wavelengths were considered (table 3). Also, correction by optical path elongation of photons travelling to the HydroScat-6 detector was minor compared with the larger variations of total backscattering ($b_b(555)$ changes up to sevenfold).

Similar to particle backscattering spectral curves, spectral shapes of total backscattering also differed between waters dominated by 'small' ($[chl_{(>20\,\mu m)}/chl_T] < 0.5$) and 'large' ($[chl_{(>20\,\mu m)}/chl_T] \geq 0.5$) phytoplankton assemblages (figure 4(*a*)). For all wavelengths, waters dominated by 'large' phytoplankton cells

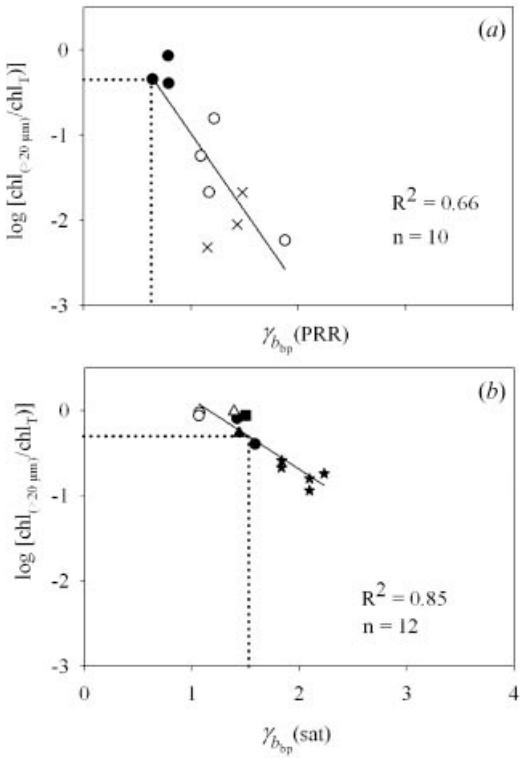

Figure 3. Semilog relationships between phytoplankton size-structure ($chl_{(>20\,\mu m)}/chl_T$) and spectral shape of particle backscattering coefficients; the spectral slope of the particle backscattering coefficient ($\gamma_{b_{bp}}$) was computed from (*a*) PRR and (*b*) satellite R_{rs} values (sat) according to Carder *et al.* (2004). Most of the points in each curve (~60%) were collected from inshore waters during 1999 (empty circles), 2000 (solid circles), 2001 (empty rectangle), 2002 (solid rectangle), 2003 (triangles), 2004 (crosses), and 2006 (stars). An exponential model of the form: $chl_{(>20\,\mu m)}/chl_T = A10^{-B\gamma_{b_{bp}}}$ was applied to field and satellite datasets, and modeled $chl_{(>20\,\mu m)}/chl_T$ values are represented as a solid line. For each curve, the $\gamma_{b_{bp}}$ threshold at which $chl_{(>20\,\mu m)}/chl_T = 0.5$ is indicated (dotted lines).

have greater b_b values with respect to those dominated by 'small' cells (~3.5-fold at 555 nm). This difference was more pronounced at wavelengths above 600 nm where chlorophyll *a* fluorescence has a significant interference on β measurements (figure 4(*a*), left axis). As expected, the greater magnitude of b_b in that cast with a larger dominance of 'large' cells ($chl_{(>20\,\mu m)}/chl_T = 0.89$) coincided with higher chl_T values ($chl_T = 13.65\,mg\,m^{-3}$) with respect to that characterized by a smaller

Table 2. Fitting parameters of empirical relationships between $chl_{(>20\,\mu m)}/chl_T$ and $\gamma_{b_{bp}}$[a].

	$Log_{10}\ A$	B	RMS log	ε_{rr}
PRR	0.834 (0.567)	−1.818 (0.466)	0.464	1.285
SeaWiFS	0.949 (0.181)	−0.8189 (0.108)	0.127	0.297

[a]The regression coefficients were obtained by linear regression of the semilog values according to the model: $chl_{(>20\,\mu m)}/chl_T = A_{10}^{-B\gamma_{b_{bp}}}$; figures in parentheses indicate one standard error.

Table 3. Path length attenuation correction of uncorrected total backscattering values estimated from HydroScat-6 measurements[a].

	Range	Average	Standard error
a_{ph}*(675)	0.05–0.166	0.055	0.017
chl_{b_b}	0.15–13.65	2.71	1.41
$chl_{b_b(>20\,\mu m)}/chl_{b_b}$	0.05–0.89	0.33	0.10
$a_g(440)\ 10^{-3}$	0.7–6.6	2.4	0.59
$\xi_g\ 10^{-3}$	5.1–15.3	9.7	1.2
$a_d(400)\ 10^{-3}$	0.3–13.6	3.4	1.4
$\xi_d\ 10^{-3}$	3.0–15.8	9.8	1.3
$\sigma(555)$	1.024–1.09	1.013	0.002
$b_b(555)\ 10^{-3}$	1.9–6.7	3.1	0.51

[a]Data were collected during January 2001. a_{ph}*(675): specific phytoplankton absorption at 675 nm ($m^2\,mg\,chl^{-1}$); chl_{b_b} and $chl_{b_b}>20\,\mu m$ are total and $>20\,\mu m$ chlorophyll *a* concentration between 0 and 10 m ($mg\,m^{-3}$); $a_g(440)$: gelbstoff absorption at 412 nm (m^{-1}); ξ_g: spectral slope of gelbstoff absorption curve between 412 and 590 nm (λ^{-1}) (Fargion and Mueller 2000); $a_d(400)$: detritus absorption at 400 nm (m^{-1}); ξ_d: spectral slope of detritus absorption between 412 and 590 nm (λ^{-1}); $\sigma(555)$ and $b_b(555)$ are the sigma factor ($\sigma=k_1\ e^{K_{exp}K_{b_b}}$; Dana and Maffione 2002) and total backscattering coefficient computed at 555 nm.

dominance of 'large' cells ($chl_{(>20\,\mu m)}/chl_T=0.05$) phytoplankton communities ($chl_T=0.15\,mg\,m^{-3}$).

Another important characteristic of spectral b_b variability on figure 4(*a*) became evident when both curves were normalized to 442 nm (the shortest spectral channel of HydroScat-6) (figure 4(*b*), right axis). Although normalized b_b values of 'small' and 'large' phytoplankton size cases increased toward the blue range, this rise was more drastic for the water with a smaller phytoplankton size-structure. In view of this fact, the slope of the $b_b(\lambda)$ spectra was calculated for all January 2001 datasets as a function of $chl_{(>20\,\mu m)}/chl_T$ by using the hyperbolic model in equation (1) (figure 4(*b*)). Similar to PRR and satellite $\gamma_{b_{bp}}$ estimations, the magnitude of HydroScat-6-derived γ_{b_b} was inversely related to log ($chl_{(>20\,\mu m)}/chl_T$) values. Consistently, a similar semi-log function between log ($chl_{(>20\,\mu m)}/chl_T$) and γ_{b_b} values was found using HydroScat-6 data (intercept$=0.47\pm0.33$, slope$=0.48\pm0.14$) and γ_{b_b} data estimated from $b_b(555)$ following Reynolds *et al.* (2001) (see equation (3); intercept$=0.66\pm0.41$, slope$=0.57\pm0.17$). Interestingly, RMS log($\sim$0.25) and ε_{rr}($\sim$0.61) values were also comparable using both approaches. After subtracting the water backscattering contribution from b_b, b_{bp} values were derived, even though no significant regressions between b_{bp} and $chl_{(>20\,\mu m)}/chl_T$ values could be obtained.

3.1.2 Total chlorophyll *a*. The second phytoplankton size-structure proxy investigated in this work was the total chlorophyll *a* concentration. Based on field $chl_{(>20\,\mu m)}$ measurements and satellite-derived chl_{DS} values, no significant relationships were detected between total and fractionated pigments (figure 5). The lack of fit was not related with the relatively small dataset resulting from satellite or PRR match-ups (figure 5(*a*)) since there was no clear pattern using the whole Pal-LTER dataset ($n=979$) either (figure 5(*b*)). Phytoplankton samples characterized by 'large' cell distributions ($[chl_{(>20\,\mu m)}/chl_T]\geqslant0.5$) were major components in both oligotrophic ($<1\,mg\,m^{-3}$) and eutrophic ($>4\,mg\,m^{-3}$) waters of the WAP region.

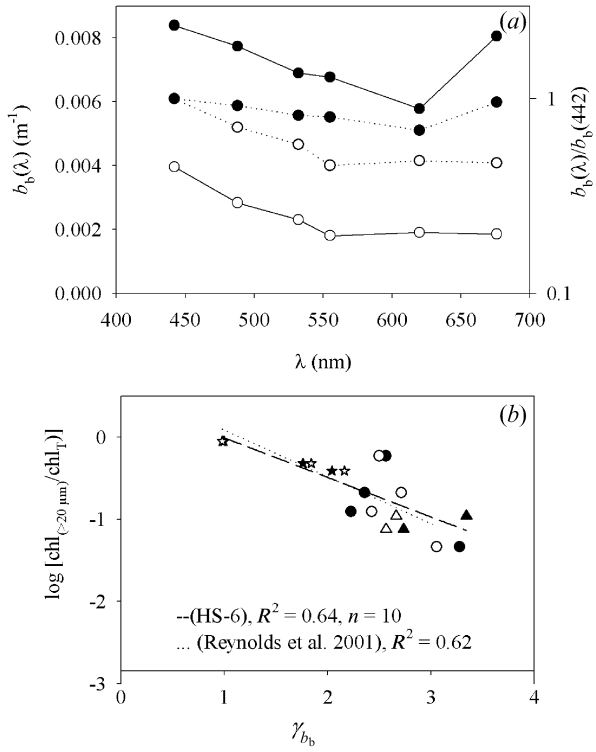

Figure 4. Spectral total backscattering as a function of phytoplankton size-structure: (*a*) mean $b_b(\lambda)$ for the top 10 m of the water column and two types of phytoplankton size distributions, left axis, and solid lines: $b_b(\lambda)$ measurements obtained from HydroScat-6 during January 2001, right axis and dotted lines: blue-normalized $b_b(\lambda)$, waters dominated by 'large cells' ([chl$_{(>20\,\mu m)}$/chl$_T$]$\geqslant$0.5, solid circles), and 'small cells' ([chl$_{(>20\,\mu m)}$/chl$_T$]$<$0.5, ○); (*b*) semilog relationship between chl$_{(>20\,\mu m)}$/chl$_T$ and spectral b_b slopes measured by HydroScat-6 (solid symbols) and estimated from $b_b(555)$ using Reynolds *et al.*'s (2001) model (empty symbols); inshore (stars), middle shelf (triangles), and shelf-break or slope (circles) waters. An exponential model of the form: $\text{chl}_{(>20\,\mu m)}/\text{chl}_T = A10^{-B\gamma_{b_b}}$ was applied to HydroScat-6 measurements and estimations based on Reynolds *et al.*'s (2001) algorithm, and modelled chl$_{(>20\,\mu m)}$/chl$_T$ values for each dataset are represented by a broken and dotted line, respectively.

3.2 *Validation of phytoplankton size-structure indices*

In a consistent way, field measurements of γ_{b_b} (HydroScat-6) and $\gamma_{b_{bp}}$ estimations based on satellite and in-water R_{rs} measurements agreed that there is a link between bulk cell size of phytoplankton communities over the WAP region, as estimated from fractionated chlorophyll *a*, and spectral characteristics of backward scattered light. Unfortunately, due to the meteorological conditions of Antarctic waters (most of the time cloudy or sea-ice covered), additional field backscattering measurements for testing these functionalities are still lacking. However, to corroborate these relationships in the field, two supplementary methods were proposed: monthly analysis of satellite-derived $\gamma_{b_{bp}}$ values and chl$_{(>20\,\mu m)}$/chl$_T$ data, and characterization of phytoplankton pigment composition. To illustrate the first method, two contrasting years were selected based on *in situ* chl$_{(>20\,\mu m)}$/chl$_T$ frequency distributions (figure 6). The January 2006 cruise was characterized by a widespread distribution of phytoplankton communities with a 'large' cell size and vice versa

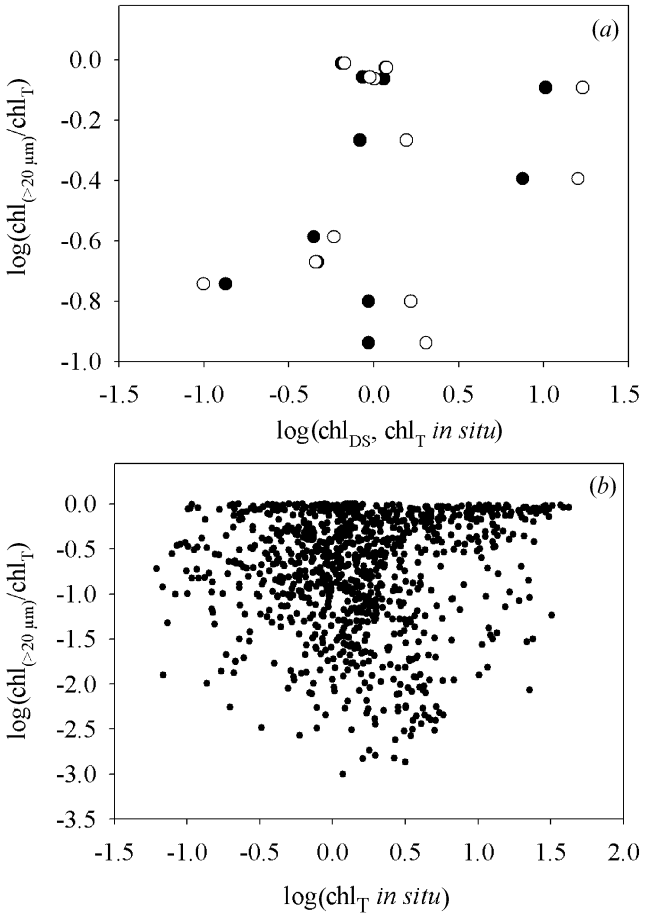

Figure 5. Semilog relationships between total and fractionated chlorophyll *a* samples over waters of the western shelf of the Antarctic Peninsula. (*a*) spatial and temporal match ups of $chl_{(>20\,\mu m)}/chl_T$ as a function of chl_{DS} (•) and field measurements (○); (*b*) dependence of $chl_{(>20\,\mu m)}/chl_T$ on chl_T values for the whole Pal-LTER dataset (n=979).

during the January 2003 cruise. Notice that spatial resolution was GAC in both cases to maintain consistency during the evaluation of the phytoplankton >20 µm binary filter. In both years, satellite-derived $\gamma_{b_{bp}}$ values evidenced smaller values (larger particle size) only over the WAP shelf and shelf-break, and in sub-Antarctic waters (figure 6(*a*) and (*c*)). The largest $\gamma_{b_{bp}}$ values (>2) were computed over those waters between the shelf-break of the WAP and sub-Antarctic waters. In general, $\gamma_{b_{bp}}$ values were lower in 2006 with respect to 2003 over the WAP shelf (0.7 vs 2) and off the shelf-break (2 vs 3) (figure 6(*c*)). Likewise, the $\gamma_{b_{bp}}$ boundary between sub-Antarctic waters and southern oceanic waters was not as well defined in January 2006 as in 2003. The binary filter for detecting waters 'rich' in large phytoplankton cells ($[chl_{(>20\,\mu m)}/chl_T] \geqslant 0.5$) is illustrated for the years 2003 and 2006 (figure 6(*b*) and (*d*)). Needless to say, the $\gamma_{b_{bp}}$ threshold distribution indicates a mean geographical position for the patch enclosed by 'large' phytoplankton (>20 µm) dominated waters (figure 3(*b*)). Based on the total integrated area of pixels (blue regions), the contribution of 'large' phytoplankton (>20 µm)-dominated waters during 2003 was

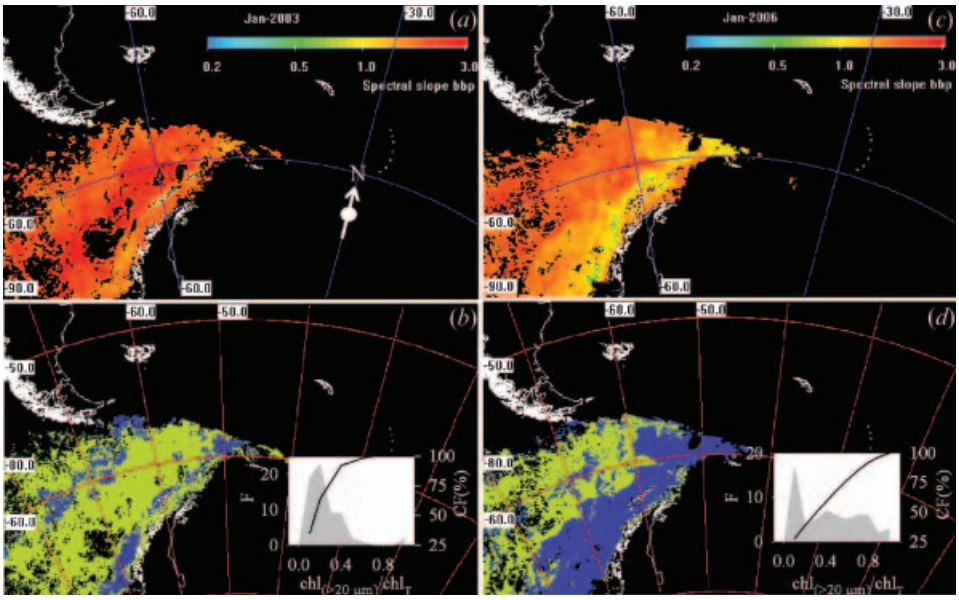

Figure 6. Validation of phytoplankton size-structure model in WAP waters based on spectral backscattering slope changes. SeaWiFS monthly composites of satellite-derived $\gamma_{b_{bp}}$ values (Carder *et al.* 2004) are depicted in (*a*) and (*c*) for typical cruise surveys where waters dominated by 'small' (January 2003) and 'large' (January 2006) phytoplankton size distributions were widely common on fractionated chlorophyll *a* samples, respectively. Binary filter of $\gamma_{b_{bp}}$ for waters where $chl_{(>20\,\mu m)}/chl_T \geqslant 0.5$ and $\gamma_{b_{bp}} \leq 1.668$ (blue pixels), and $[chl_{(>20\,\mu m)}/chl_T] < 0.5$ and $\gamma_{b_{bp}} > 1.668$ (green pixels) computed for January 2003 (*b*) and January 2006 (*d*) cruise. Based on field samples, histograms of $chl_{(>20\,\mu m)}/chl_T$ values are depicted for January of each year (inset of panel (*b*) and (*d*)), where the frequency distribution (*F*) is indicated by a grey area (left axis), and the cumulative frequency probability (CF%=100 [number of observations per bin/total number of observations]), right axis) is symbolized as a continuous line. Image composites are drawn using a conic Lambert projection.

one-fifth of that computed for 2006. Histograms of $chl_{(>20\,\mu m)}/chl_T$ field measurements confirmed this remarkable difference between years (figure 6(*b*) and (*d*), lower right inset). In 2003, about 92% of the $chl_{(>20\,\mu m)}/chl_T$ observations were concentrated in the 0.3–0.4 bin (60 data, $n=65$, cumulative distribution). In 2006, only 54% of the field measurements (33 data, $n=61$) were counted in the same bin. Another important difference between 2003 and 2006 years regarding the $\gamma_{b_{bp}}$ threshold was the horizontal distribution of values below 1.668 (i.e. those dominated by >20 µm cells) which were almost concentrated along the shelf-break in 2003 and widespread over inshore, shelf, and shelf-break waters in 2006.

The performance of the $\gamma_{b_{bp}}$ binary mask to discriminate phytoplankton assemblages with a different size-structure was evaluated for different WAP zones and years using all data collected by ship surveys. Although these datasets did not necessarily correspond in time with satellite measurements, the ability to distinguish areas with dominance of 'large' vs 'small' phytoplankton cell size classes was exemplary ($\varepsilon_{Filter\ (>20\,\mu m)}=21\%$) (table 4). False hits were connected to sampling aliasing in those areas with the highest spatial variability and misrepresentation of satellite-derived $\gamma_{b_{bp}}$ values in the monthly scale (figure 7). For instance, for January 2006, a likely mismatch occurred in those areas with a small number of satellite observations per pixel (figure 7(*a*)) and/or with the largest spatial variability (figure 7(*b*)).

Table 4. Statistical results for the performance of the phytoplankton size-structure model based on spectral backscattering slope changes[a].

Year	Line	WR	mchlf	se1	mechlf	Fchlf	n1	mchl	se2	mechl	Fp20	np
1999	600	I	0.93	0.05	0.98	**1.00***	8	0.98	0.19	1.08	**0.00***	8
	200		0.93	0.02	0.94	1.00	4	1.09	0.14	1.11	1.00	4
2000	600	I	0.03	0.02	0.03	0.00	4	1.04	0.45	1.05	0.00	2
	200		0.35	0.06	0.34	0.00	2	1.30	1.06	1.30	0.00	2
	200	M	0.21	0.04	0.21	0.00	2	0.66	0.07	0.66	0.00	2
	600	S	0.19	0.09	0.15	0.00	3	0.12	0.02	0.13	0.00	3
2001	200	I	0.58	0.11	0.59	0.50	4	3.04	0.98	2.63	0.75	3
	600	M	0.09	0.01	0.09	0.00	3	2.30	0.40	2.48	0.33	3
	600	S	0.17	0.04	0.17	0.00	2	1.26	0.93	1.26	0.00	2
2003	600	I	0.05	0.02	0.03	0.00	3	2.06	0.20	2.05	0.00	2
	200		0.22	0.13	0.12	**0.14***	7	1.13	0.12	1.27	**0.58***	6
	600	M	0.04	0.05	0.02	0.00	4	1.19	0.33	1.44	0.00	4
	200		0.13	0.04	0.13	0.00	4	0.39	0.10	0.42	0.25	4
	600	S	0.20	0.02	0.21	0.00	6	0.17	0.03	0.15	0.00	6
	200		0.21	0.08	0.12	0.00	3	0.11	0.01	0.12	0.00	3
2004	600	I	0.03	0.03	0.01	0.00	3	3.81	7.00	1.17	0.00	3
	200		0.54	0.01	0.52	**1.00***	2	0.72	0.01	0.72	**0.00***	2
	600	M	0.03	0.02	0.02	0.00	3	3.46	0.85	4.13	0.00	4
	200		0.59	0.11	0.51	0.75	4	0.48	0.05	0.51	0.67	3
	600	S	0.09	0.02	0.10	0.00	4	0.60	0.36	0.27	0.00	4
	200		0.45	0.06	0.45	0.50	2	0.32	0.03	0.32	0.00	2
2005	600	I	0.03	0.01	0.03	0.00	4	2.46	0.24	2.61	0.29	4
	200		0.32	0.13	0.23	0.38	7	10.19	3.50	7.33	0.00	4
	600	M	0.02	0.01	0.01	0.00	4	1.17	0.24	1.17	0.33	3
	200		0.01	0.01	0.01	**0.00***	4	2.70	0.54	3.20	**1.00***	4
	600	S	0.02	0.01	0.02	0.00	6	0.49	0.19	0.36	0.00	5
	200		0.05	0.02	0.06	0.00	3	0.52	0.38	0.15	0.00	3
2006	600	I	0.17	0.16	0.03	0.00	3	3.54	0.98	3.89	0.20	3
	200		0.72	0.09	0.79	**0.80***	5	8.95	0.80	8.73	**0.40***	5
	600	M	0.11	0.07	0.06	**0.00***	4	5.00	1.64	3.65	**1.00***	4
	200		0.78	0.08	0.79	1.00	4	8.44	1.63	8.53	1.00	4
	600	S	0.22	0.16	0.07	**0.25***	4	1.69	0.67	1.20	**1.00***	4
	200		0.40	0.05	0.41	0.17	6	0.49	0.07	0.49	1.00	6

[a]Line is the sampling transect (Pal-LTER grid) which is across the WAP shelf; WR: regions within the Pal-LTER study area; I: inshore; M: middle shelf; S: shelf-break or slope; mchlf: average of $chl_{(>20\,\mu m)}/chl_T$ samples and its standard error (se1) and number of samples (n1); mechlf: median of $chl_{(>20\,\mu m)}/chl_T$ samples; Fchlf: proportion of number of field measurement that were greater or equal to 0.5; mchl: average of chl_T samples ($mg\,m^{-3}$) and its standard error (se2); mechl: median of chl_T samples in $mg\,m^{-3}$; Fp20: proportion of number of satellite measurements where $\gamma_{b_{bp}} \leq 1.668$ (i.e. $[chl_{(>20\,\mu m)}/chl_T] \geqslant 0.5$); the number of stations with valid pixels (np) is summarized in the last column. Mismatch between satellite and field data is shown by an asterisk. Comparisons with only one sample were excluded.

The second tool used to confirm the consistency of $\gamma_{b_{bp}}$ as an index of phytoplankton size-structure over the WAP region was the analysis of phytoplankton photosynthetic pigment signatures. Fucoxanthin and 19′-BF were the only pigment markers that had a significant relationship with satellite-derived $\gamma_{b_{bp}}$ values (figure 8(*a*) and (*b*)). In both cases, there was an inverse relationship but 19′-BF ($19'\text{-BF} = -0.048 \pm 0.012\gamma_{b_{bp}} + 0.111 \pm 0.020$, RMS log=0.16, ε_{rr}=0.37) had a better linear fit than fucoxanthin (fucoxanthin $= -0.072 \pm 0.032\gamma_{b_{bp}} + 0.217 \pm 0.055$, RMS log=0.21, ε_{rr}=0.50). Consistently, further analysis using b_b measurements from HydroScat-6 also evidenced a selective influence of these pigments on

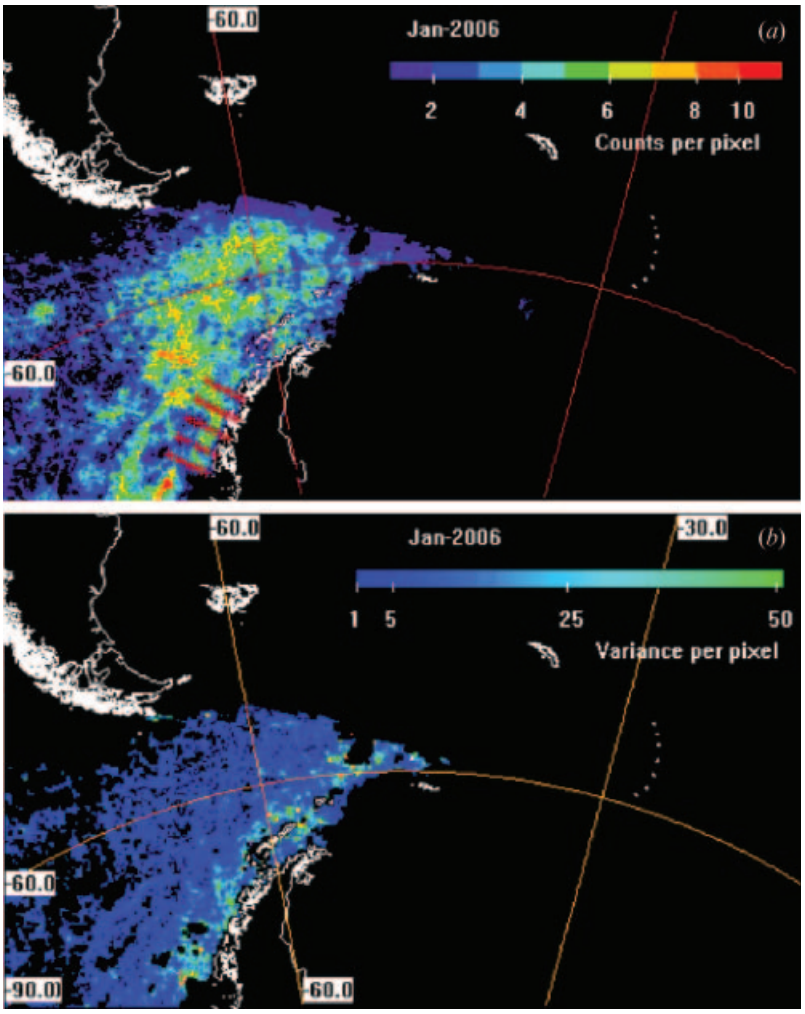

Figure 7. Spatial variability on statistical parameters of satellite-derived spectral particle backscattering slope. The case study corresponds to January 2006, so the GAC imagery was processed: (*a*) number of images with valid data per pixel used for the monthly composite (nominal sampling grid stations shown as red crosses); (*b*) variance of satellite observations of $\gamma_{b_{bp}}$ per pixel.

γ_{b_b} values ($19'\text{-BF} = -0.249 \pm 0.09\gamma_{b_b} + 0.767 \pm 0.222$, RMS log=0.39, ε_{rr}=1.02, fucoxanthin $= -1.669 \pm 0.664\gamma_{b_b} + 5.27 \pm 1.64$, RMS log=0.30, ε_{rr}=0.73) (figure 8(*c*) and (*d*)). No comparisons could be made between PRR-derived $\gamma_{b_{bp}}$ values and HPLC pigments because of the reduced number of matchups ($n<3$). Other major (alloxanthin and 19′-hexanoylofucoxanthin) and minor (chlorophyll *b*, peridinin) phytoplankton signatures over WAP waters seemed to vary independently from changes on spectral backscattering characteristics of particles.

4. Discussion

The WAP region has been undergoing remarkable ecological changes in the last decade (e.g. decline of Adelie penguin; Fraser and Patterson 1997) that could be

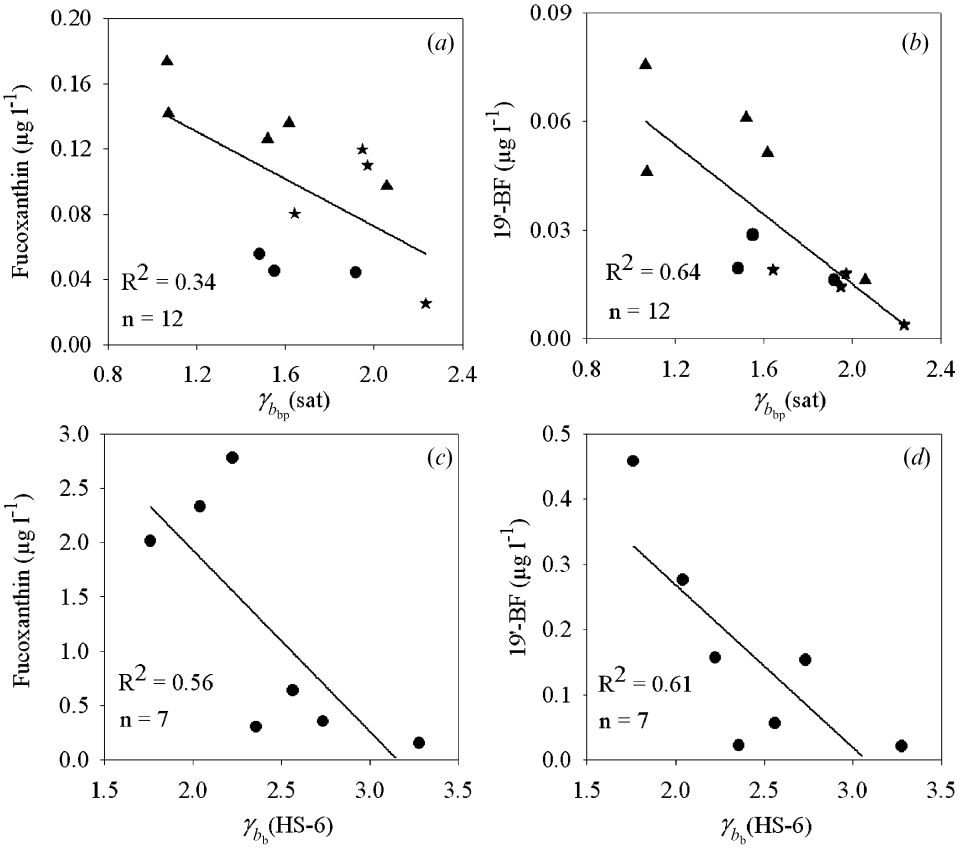

Figure 8. Relationships between phytoplankton photosynthetic signatures and spectral slopes of satellite-derived (sat) particle backscattering, and HydroScat-6 (HS-6)-derived total backscattering. (*a*) fucoxanthin vs $\gamma_{b_{bp}}$; (*b*) 19′-butanoyloxyfucoxanthin or 19′-BF vs $\gamma_{b_{bp}}$; (*c*) fucoxanthin vs γ_{b_b}; (*d*) 19-butanoyloxyfucoxanthin or 19′-HF vs γ_{b_b}. Linear regressions are shown with a solid line. HPLC data corresponded to January of 1998 (circles), 1999 (triangles), and 2003 (stars). Fifty per cent of the stations were over slope waters.

attributed to modifications of lower trophic levels such as the replacement of phytoplankton communities dominated by 'large' cells' (e.g. diatoms >20 μm) by communities dominated by 'small cells' (e.g. microflagellates) (Moline *et al.* 2004a). Due to the harsh and changing meteorological conditions of Antarctic waters, summer shipboard surveys are challenging and may not be enough to characterize the true variability of the phytoplankton size-structure over large regions. Therefore, there is an urgent need to develop synoptic and global coverage tools such as satellite algorithms to monitor ecological trends on phytoplankton communities of WAP waters. In this work, existing optical models were applied to investigate potential relationships between total chlorophyll *a* concentration, particle size distribution and phytoplankton size-structure over the WAP region and adjacent marine areas. Reflectance-based models of chl_T (equation (4)) and particle size distribution (equations (2) and (3)) were used as indices of the mean bulk cell size of phytoplankton assemblages.

In the next section, the physics and optical components behind the bio-optical relationship between optical indices ($\gamma_{b_{bx}}$, chl_{DS}) and phytoplankton size-structure,

closure between different backscattering measurements and phytoplankton bulk cell size characteristics, and validation of backscattering indices of the phytoplankton size-structure will be analysed.

4.1 *Physics and optical components behind the bio-optical relationship between* γ_x, $\mathbf{chl_{DS}}$, *and phytoplankton size-structure*

The spectral slope of the particle and total backscattering were the first type of optical index tested in this work to retrieve the size-structure of phytoplankton assemblages of the WAP. In a consistent way, significant functionalities were obtained between $\gamma_{b_{bp}}$, γ_{b_b} and phytoplankton chlorophyll *a* fractions (figures 3 and 4), and this implies that changes in the phytoplankton size-structure affect the spectral characteristics of backscattered light in Antarctic waters of the WAP region. This fact is particularly intriguing given that most of the total backscattering in the ocean is believed to have originated from non-phytoplankton particles such as detritus and colloidal components (Stramski *et al.* 2001, Stramski and Wozniak 2005). Whether the inverse relationship observed between $\mathrm{chl}_{(>20\,\mu m)}/\mathrm{chl}_T$ and spectral backscattering slopes was caused by different phytoplankton or phytoplankton-derived detritus size distributions is not known. For the Southern Ocean, a general correlation between a_{ph}, a_d, and a_g values has been pointed out (Mitchell and Holm-Hansen 1991, Reynolds *et al.* 2001) and supports the fact that phytoplankton biomass and their metabolic dissolved and particle organic compounds are interdependent. Hence, it is not unrealistic to think that larger phytoplankton communities might be a source of larger particles populations and vice versa. Unfortunately, as pointed out by Stramski *et al.* (2004), no measurements of backscattering of 'well-characterized' organic detritus particles isolated from ocean waters have been made. Furthermore, inorganic particles of terrigenous origin could not be responsible for the spectral backscattering variability observed during comparisons because the near-shore bio-optical domain, highly influenced by glacial silt, was not included in the scope of the present study.

Unlike cell size, the potential influence of other phytoplankton community characteristics such as cell shape and composition on spectral $\gamma_{b_{bx}}$ variability might be expected to be minor, since these last parameters have a narrow range of variation (e.g. index of refraction; Ahn *et al.* 1992) or affect greatly other optical properties of phytoplankton such as the backscattering efficiency for a given wavelength (Quirantes and Bernard 2004).

Another important result of this work was that 'large' phytoplankton cells (>20 μm) had the strongest influence shaping spectral b_b and b_{bp} curves as $\left[\mathrm{chl}_{(>20\,\mu m)}/\mathrm{chl}_T\right]-\gamma_{b_{bx}}$ curves and phytoplankton photosynthetic pigment markers revealed. Mechanistically, the dependence of $\mathrm{chl}_{(>20\,\mu m)}/\mathrm{chl}_T$ on $\gamma_{b_{bp}}$ can be clearly related to $R_{rs}(443)/R_{rs}(488)$ changes (equation (2)). When phytoplankton communities are populated by smaller cells, upwelling light leaving the sea-surface becomes blue-enriched. In other words, smaller particles, including phytoplankton, will tend to scatter shorter wavelengths. This spectral switch was not caused by light absorption modifications as shown by K_d, a quasi-inherent optical property highly dependent on *a* (figure 2(*b*)). Also, spectral changes in R_{rs} due to variations of phytoplankton biomass would be expected to be minor, since these changes are evident at longer wavelengths (~555 nm) (figure 2(*a*)).

Based on experimental and theoretical (Mie theory) spectral backscattering efficiency factors ($\overline{Q_{b_b}} = b_b\left[\pi/4\int_0^\infty F(D)D^2\mathrm{d}(D)\right]^{-1}$, where $F(D)d(D)$ was the number

of cells per cubic metre in the diameter interval D to $D+d(D)$ per cell) of nine phytoplankton species, Ahn *et al.* (1992) consistently found that $\overline{Q_{b_b}}$ for very small cells had almost no spectral dependence, since $\overline{Q_{b_b}}$ varies as λ^{-2}. For the same reason, relatively small optical constituents such as colloids and detritus might exert a minor effect on spectral backscattering shapes. Conversely, large cells present more featured $\overline{Q_{b_b}}$ spectra because of the effect of absorption upon backscattering. This phenomenon is predicted by the anomalous dispersion theory and is more evident in those spectral regions near absorption bands (e.g. 440 and 675 nm for phytoplankton; Van de Hulst 1957). In this work, b_b spectra determined with HydroScat-6 had a characteristic monotonic increase from long to short wavelengths, as previously observed with lab $\overline{Q_{b_b}}$ measurements of phytoplankton cultures (Vaillancourt *et al.* 2004) and *in situ* b_{bp} spectra in the Baltic Sea (Aas *et al.* 2005). In contrast, Mie theory calculations of $\overline{Q_{b_b}}$ for different phytoplankton species suggested an opposite trend (Ahn *et al.* 1992). This apparent discrepancy is mainly explained by the fact that Mie inversion calculations assume spherical and monodisperse particle populations following Junge-type size distributions. Increasing evidence based on more complicated scattering models (e.g. coated spheres, spheroids; Gordon and Du 2001, Quirantes and Bernard 2004) and *in situ* measurements of particle spectra (e.g. polydisperse and log-normal distributions; Twardowski *et al.* 2004) have shown that Mie theory assumptions are currently not met in nature.

The second type index proposed to distinguish changes on phytoplankton size-structure of WAP waters was the total concentration of chlorophyll *a*. Overall, neither *in situ* measurements nor satellite chl_T estimates using Dierssen and Smith's (2000) algorithm were successfully linked to $chl_{(>20\,\mu m)}/chl_T$ variability. Conversely, Bidigare *et al.* (1996) stated that chlorophyll-rich waters are associated with abundant 'large' phytoplankton cells. As noticed by Garibotti *et al.* (2003a), this pattern is not always true over the Pal-LTER research site. Most important phytoplankton blooms in Antarctic waters may be originated by phytoplankton classes with mean cell size distributions larger than 20 μm (e.g. large diatoms like *Coscinodiscus bouvet*) or smaller than 10 μm (e.g. cryptophytes) (Garibotti *et al.* 2005). Therefore, chl_T or chl_{DS} is an ambiguous index and cannot be used as a reliable proxy of phytoplankton cell size spectra.

4.2 *Closure between different backscattering measurements and phytoplankton bulk cell size characteristics*

The link between spectral backscattering characteristics and phytoplankton size-structure was consistently checked with satellite-derived and *in situ* measurements of reflectance using a global model of $\gamma_{b_{bp}}$, and *in situ* spectral measurements of total backscattering. Although an inverse mathematical function described both satellite and PRR reflectance $-\gamma_{b_{bp}}$ relationships, the slope of the linear regression was significantly different between them. This apparent discrepancy could possibly be attributed to the field-of-view and sampling timing differences between the two sensors. Match-ups between *in situ* R_{rs} measurements and $chl_{(>20\,\mu m)}/chl_T$ values were almost concurrent (within 30 min) and spatially coincident while satellite-derived R_{rs} measurements were collected within 4 h of the ship survey and corresponded to an area between 3 and 9 km^2. Another explanation for such an apparent discrepancy between the slopes of $\gamma_{b_{bp}} - chl_{(>20\,\mu m)}/chl_T$ *in situ* and satellite relationships could be related to the fact that match-up dates of field and satellite measurements were not necessarily the same because of the methodological

differences between PRR and space sensors to define clear vs cloudy conditions. Sky pictures taken by a camera were used to detect overcast days during PRR determinations while SeaWiFS 'cloudy' pixels were flagged out based on a reflectance threshold. Since satellite match-up is made with a filter of ten (LAC images) or five (GAC) pixels, the probability of finding pixels not fully cloudy is greater with respect to field measurements. Likewise, part of the discrepancy comparing field and satellite data is caused by the temporal mismatch of satellite passes (e.g. no 2004 SeaWiFS imagery was collected within 4 h of the ship surveys).

In the visible range, *in situ* measurements of total spectral backscattering also supported the optical functionality found with $\gamma_{b_{bp}}$ estimates (i.e. larger γ_{b_b} values when particles/phytoplankton size distributions are smaller). Furthermore, calculations of γ_{b_b} were very consistent with those derived from HydroScat-6 measurements of $b_b(555)$ and using the empirical model developed for Ross Sea and Antarctic front waters using the same optical instrumentation (equation (3); Reynolds *et al.* 2001). This remarkable agreement between the two $\mathrm{chl}_{(>20\,\mu m)}/\mathrm{chl}_T - \gamma_{b_b}$ relationships (figure 4(*b*)) showed that $\mathrm{chl}_{(>20\,\mu m)}/\mathrm{chl}_T - \gamma_{b_b}$ functionality obtained in this study might also be valid in other Antarctic waters besides the WAP region.

Similar to semi-analytical expressions based on Mie theory (Ahn *et al.* 1992, Stramski *et al.* 2001), calculation of b_b from HydroScat-6 measurements is approximated. For a fixed scattering angle, b_b and β values were related in this work with a dimensionless coefficient χ, which was assumed wavelength-independent for scattering angles between 100 and 150°, and has implicit water and particle contributions (Dana and Maffione 2002). For scattering angles below 120°, the conversion factors for the total (χ) and particle (χ_p) component are the same (Boss and Pegau 2001). However, at angles above 110°, χ departs significantly from χ_p due to a larger influence of the pure seawater contribution to β (Chami *et al.* 2006). Based on volume scattering function measurements using phytoplankton cultures, even greater spectral differences on χ may be observed during phytoplankton blooms, since χ_p is very sensitive to size distribution of particles. These authors found that spectral variations of χ_p corresponding with uncertainties of circa 10% and 25% on b_b might be expected for non-blooming oceanic waters and phytoplankton bloom conditions, respectively. Although significant, this error was minor with respect to the largest differences computed on γ_{b_b} in waters with varied $\mathrm{chl}_{(>20\,\mu m)}/\mathrm{chl}_T$ (0.05–0.85%, figure 4(*b*)) ($\Delta\gamma_{b_b}$ of normalized values up to 155%).

4.3 *Validation of backscattering indices of phytoplankton size-structure*

In this work, functionality between $\mathrm{chl}_{(>20\,\mu m)}/\mathrm{chl}_T$ and $\gamma_{b_{bp}}$ values was first verified with a binary filter based on a chlorophyll *a* size fraction cutoff ($\gamma_{b_{bp}}$ value when $\mathrm{chl}_{(>20\,\mu m)}$ exceeds or equal 50% of relative contribution to chl_T) and applied to SeaWiFS imagery. This supervised classification method is an approximation, which implies that detection of waters dominated by 'large' phytoplankton will occur when that community accounts for the largest portion of biomass in the sample. A binary filter was used instead of a continuous distribution of $\gamma_{b_{bp}}$ to map spatial changes on phytoplankton size-structure of WAP waters for three reasons: (1) the $\mathrm{chl}_{(>20\,\mu m)}/\mathrm{chl}_T - \gamma_{b_{bp}}$ algorithm was designed to discriminate microphytoplankton (>20 μm) from pico/nanophytoplankton (<20 μm), main phytoplankton size classes driven food webs (diatom-based vs flagellate-based) in Antarctic waters (Walsh *et al.* 2001); (2) more data are needed to minimize time–space mismatch of $\gamma_{b_{bp}}$ index validations and obtain a greater number of size classes categories; (3) an implicit

error of $chl_{(>20\,\mu m)}/chl_T$ estimation will limit the number of reliable size classes categories estimated.

Despite the time–space mismatches between field and satellite observations in the monthly scale, the binary filter had a very accurate performance (efficiency ~80%) to differentiate waters chlorophyll-dominated by >20 μm cells during January of several years and different WAP regions (table 4, figure 6). Given that main phytoplankton assemblages of the WAP (diatoms and cryptophytes) have a different size-structure and are strongly affected by the timing of sea-ice retreat (Garibotti *et al.* 2003a, 2005), a high-ice year (2006) and low-ice year (2003) were chosen to confirm the ability of the binary filter. By December 2006, the sea-ice extent (i.e. sea-ice area enclosed by the 15% sea-ice concentration contour, km^2) (Smith and Stammerjohn 2001) was 27% higher than that estimated with satellite data (SMMR-SSM/I) in 2003 for the same period (Dr. Sharon Stammerjohn, pers. comm.). Therefore, and based on microscopic observations (Garibotti *et al.* 2003a, 2005), a large bloom of large diatoms might be expected during the high ice year (2006) due to a higher water-column stability during the summer (Mitchell and Holm-Hansen 1991) caused by a greater sea-ice extent in the previous winter and a larger delay on sea ice retreat in the previous spring (Smith and Stammerjohn 2001). In figure 6, the binary filter showed that 'large cells' dominated during 2006 principally throughout coastal and middle shelf waters of the WAP. Notice that some 'large cells' patches were also detected offshore the continental shelf (a more continuous feature in 2003). These distributions may correspond with large or long-chained diatom blooms (e.g. *Thalassiothrix* spp.) characteristics of the Antarctic Polar Front (Smetacek *et al.* 2002, Tremblay *et al.* 2002). During the summer seasons with a low sea-ice extent such as 1997 and 1999, 'small size cell' phytoplankton communities (unidentified flagellates-cryptophytes and small-open water diatoms such as *Fragillariopsis* spp.) inhabit most of the inshore, middle shelf, and shelf-break slope waters of the WAP (Rodriguez *et al.* 2002, Garibotti *et al.* 2003a). In January 2003, pixels flagged with a high contribution of $chl_{(>20\,\mu m)}$ were computed around Renauld Island and north of Anvers Island where coastal large solitary or long-chained diatoms, colonial prymnesiophytes (*Phaeocystis* spp.), and large prasinophytes (*Pyramimonas* spp.) were not abundant (figure 1, Garibotti *et al.* 2003a).

The analysis of $\gamma_{b_{bp}}$ and γ_{b_b} variability as a function of principal photosynthetic pigment markers over the study area was the second tool used to determine the suitability of $b_b(\lambda)$ and $b_{bp}(\lambda)$ spectra as an index of the size-structure of WAP phytoplankton communities. The implicit assumption of backscattering-pigment marker relationships is that changes on pigment marker due to phytoplankton photo-acclimation over the WAP region are negligible with respect to those changes caused by a greater abundance of phytoplankton cells. Garibotti *et al.* (2003b) found no evidence of changes in cell pigment ratios due to light variations in the three phytoplankton assemblages mentioned above, and this result may be expected in other areas as well, since phytoplankton growth is closely related to local environmental conditions (Smith and Sakshaug 1990).

Unsurprisingly, fucoxanthin, the pigment signature of one of the phytoplankton classes with the largest cells (diatoms) was inversely related to spectral backscattering slope values. Although fucoxanthin is well correlated with diatom abundances over the Pal-LTER grid (Garibotti *et al.* 2003b), other phytoplankton classes (chrysophytes, raphydophytes, and pelagophytes) could also share this photosynthetic pigment marker (Rodriguez *et al.* 2002). However, and based on the

literature, no blooms of these taxonomic groups have ever been reported for WAP waters. An unexpected finding resulted when the pigment marker of type IV prymnesiophytes (19′-BF) covaried in a negative way with $\gamma_{b_{bx}}$ values. Although type IV prymnesiophytes are characterized by relatively small flagellate cells ($<3\,\mu m$), the most abundant species of this taxonomic group in Antarctic waters (*Phaeocystis* sp.) can form large colonies with diameters 50–1000 μm, easily above 20 μm (Hong *et al.* 1997). Since *Phaeocystis* sp. starts growing in spring, and the colony-formation mechanism is basically triggered by nutrient limitation (phosphates), it is probable that a significant proportion of pixels flagged 'large cells' over Marguerite Bay during phosphate-poor conditions of summer (January) represented *Phaeocystis* sp. aggregates. Greater abundances of *Phaeocystis* sp. are commonly observed not only in Marguerite Bay but in other areas of the Southern Ocean such as the Bransfield Strait and Ross Sea (Hong *et al.* 1997, Rodriguez *et al.* 2002).

5. Summary and conclusions

This work has first attempted to classify phytoplankton communities on Antarctic waters based on size-structure indices. Unlike absorption algorithms where phytoplankton size fractions are categorized according to their physiological (Ciotti *et al.* 1999) or pigment characteristics (Vidussi *et al.* 2001, Bricaud *et al.* 2004), the approach proposed in this research is independent of phytoplankton photoacclimation or pigment composition. Thus, more direct estimates are obtained, since phytoplankton size classes are differentiated according to their spectral backscattering differences similar to those size distributions of total particles. The main intention of this study was to determine the relationships between two remote-sensing products (spectral backscattering slopes of b_b and b_{bp} and chl_T) and phytoplankton size-structure variations on waters west of the Antarctic Peninsula. Although this study did not directly quantify phytoplankton cell size distributions, predictable changes on $\gamma_{b_{bx}}$ due to phytoplankton assemblages with different size fractions were consistently demonstrated. The global model to calculate the slope of spectral particle backscattering was a satisfactory index for estimating phytoplankton cell size distributions over the Pal-LTER grid and other adjacent marine waters such as Bellinghausen and Drake Sea. The phytoplankton size-structure index developed in this study will be applied in the future to study long-term trends in phytoplankton communities of WAP waters.

Acknowledgements

This work was supported by the National Science Foundation (OPP-90-11927, OPP-96-32763, OPP-02-17282) and NASA funding (NNG04GL55G; KLC). We thank Wendy Kozlowski, Karie Sines, Karen Pettersen, and Karen Baker for technical assistance, data access, and field surveys. We thank Dr. Scott Pegau for sharing HydroScat-6 during field surveys. Also, we thank Heidi Dierssen for collecting optical measurements. This study is Palmer-LTER contribution #0289.

References

Aas, E., Høkedal, J. and Sorensen, K., 2005, Spectral backscattering coefficient in coastal waters. *International Journal of Remote Sensing*, **26**, pp. 331–343.

Ahn, Y.H., Bricaud, A. and Morel, A., 1992, Light backscattering efficiency and related properties of some phytoplankters. *Deep-Sea Research*, **39**, pp. 1835–1855.

BIDIGARE, R.R., IRIARTE, J.L., KHAN, S.H., KARENTZ, D., ONDRUSEK, M.E. and FRYXELL, G.A., 1996, Phytoplankton: qualitative and quantitative assessments. In *Foundations for Ecosystem Research in the Western Antarctic Peninsula Region*, R. Ross, E. Hoffmann and L. Quetin (Eds), pp. 173–198 (Washington, DC: American Geophysical Union).

BOSS, E. and PEGAU, S., 2001, Relationship of light scattering at an angle in the backward direction to the backscattering coefficient. *Applied Optics*, **40**, pp. 5503–5507.

BRICAUD, A. and MOREL, A., 1986, Light attenuation and scattering by phytoplanktonic cells: A theoretical modeling. *Applied Optics*, **25**, pp. 571–580.

BRICAUD, A., CLAUSTRE, H., RAS, J. and OUBELKHEIR, K., 2004, Natural variability of phytoplanktonic absorption in oceanic waters: Influence of the size structure of algal populations. *Journal of Geophysical Research*, **109**, c11010.

CARDER, K., CHEN, F.R., LEE, Z. and HAWES, S., 1999a, *MODIS ATBD-19 v.5* (Washington, DC: NASA).

CARDER, K.L., CHEN, F.R., CANNIZZARO, J.P., CAMPBELL, J.W. and MITCHELL, B.G., 2004, Performance of the MODIS semi-analytical ocean color algorithm for chlorophyll-a. *Advances in Space Research*, **33**, pp. 1152–1159.

CARDER, K.L., CHEN, F.R., LEE, Z.P. and HAWES, S.K., 1999b, Semianalytical Moderate-Resolution Imaging Spectrometer algorithms for chlorophyll a and absorption with bio-optical domains based on nitrate-depletion temperatures. *Journal of Geophysical Research*, **104**, pp. 5403–5421.

CARDER, K.L., STEWARD, R.G., PAUL, J.H. and VARGO, G.A., 1986, Relationships between chlorophyll and ocean color constituents as they affect remote-sensing models. *Limnology Oceanography*, **31**, pp. 403–413.

CHAMI, M., MARKEN, E., STAMNES, J.J., KHOMENKO, G. and KOROTAEV, G., 2006, Variability of the relationship between the particulate backscattering coefficient and the volume scattering function measured at fixed angles. *Journal of Geophysical Research*, **11**, c05013.

CIOTTI, A.M., CULLEN, J.J. and LEWIS, M.R., 1999, A semi-analytical model of the influence of phytoplankton community structure on the relationship between light attenuation and ocean color. *Journal of Geophysical Research*, **104**, pp. 1559–1578.

COLLIER, J.L., 2000, Flow cytometry and the single cell in phycology. *Journal of Phycology*, **36**, pp. 628–644.

DANA, D.R. and MAFFIONE, R.A., 2002, Determining the backward scattering coefficient with fixed-angle backscattering sensors—revisited. In *Proceedings of Ocean Optics XVI*, 18–22 November 2002, Santa Fe, NM.

DIERSSEN, H.M. and SMITH, R.C., 2000, Bio-optical properties and remote sensing ocean color algorithms for Antarctic Peninsula waters. *Journal of Geophysical Research*, **105**, pp. 26, 301–326, 312.

DIERSSEN, H.M., SMITH, R.C. and VERNET, M., 2002, Glacial meltwater dynamics in coastal waters west of the Antarctic Peninsula. *Proceedings of the National Academy of Sciences*, **99**, pp. 1790–1795.

FARGION, G.S. and MUELLER, J.L., 2000, Ocean optics protocols for Satellite Ocean color sensor validation, revision 2. NASA Technical Memorandum 209966, SeaWiFS Technical Report Series, Chapter 2. Determination of spectral absorption coefficients of particles, dissolved material and phytoplankton for discrete water samples (Greenbelt, MD: NASA/TM-2000-209966, Goddard Space Flight Space Center).

FLORY, E.N., HILL, P.S., MILLIGAN, T.G. and GRANT, J., 2004, The relationship between floc area and backscatter during a spring phytoplankton bloom. *Deep-Sea Research I*, **51**, pp. 213–223.

FRASER, W.R. and PATTERSON, D.L., 1997, Human disturbance and long-term changes in Adelie penguin populations: a natural experiment at Palmer Station, Antarctica Peninusla. In *Antarctic Communities: Species, Structure and Survival*, B. Battaglia, J.

Valencia and D.W.H. Walton (Eds), pp. 445–452 (Cambridge: Cambridge University Press).

GARIBOTTI, I.A., VERNET, M., FERRARIO, M.E., SMITH, R.C., ROSS, R.M. and QUETIN, L.B., 2003a, Phytoplankton spatial distribution patterns along the western Antarctic Peninsula (Southern Ocean). *Marine Ecology Progress Series*, **261**, pp. 21–39.

GARIBOTTI, I.A., VERNET, M., KOZLOWSKI, W.A. and FERRARIO, M.E., 2003b, Composition and biomass of phytoplankton assemblages in coastal Antarctic waters: a comparison of chemotaxonomic and microscopic analyses. *Marine Ecology Progress Series*, **247**, pp. 27–42.

GARIBOTTI, I.A., VERNET, M., SMITH, R.C. and FERRARIO, M.E., 2005, Interannual variability in the distribution of the phytoplankton standing stock across the seasonal sea-ice zone west of the Antarctica Peninsula. *Journal of Plankton Research*, **27**, pp. 825–843.

GORDON, H.R., BROWN, J.W., BROWN, O.B., EVANS, R.H. and CLARK, D.K., 1988, Exact Raleigh scattering calculations for use with Nimbus-7 coastal zone color scanner. *Applied Optics*, **27**, pp. 862–871.

GORDON, H.R. and DU, T., 2001, Light scattering by nonspherical particles: Application to coccoliths detached from *Emiliana huxleyi*. *Limnology and Oceanography*, **46**, pp. 1438–1454.

GORDON, H.R. and MCCLUNEY, W.R., 1975, Estimation of the depth of sunlight penetration in the sea for remote sensing. *Applied Optics*, **14**, pp. 413–416.

GORDON, H.R. and MOREL, A., 1983, *Remote Assessment of Ocean Color for Interpretation of Satellite Visible Imagery: a Review* (New York: Springer).

GORDON, H.R., SMITH, R.C. and ZANAVELD, J.R.V., 1980, Introduction to ocean optics. In *Ocean Optics VI*, S.Q. Duntley (Ed.). Proc. SPIE, **208**, pp. 1–43.

GREEN, R.E. and SOSIK, H.M., 2004, Analysis of apparent optical properties and ocean color models using measurements of seawater constituents in New England continental shelf surface waters. *Journal of Geophysical Research*, **109**, pp. 1029.

HONG, Y., SMITH, W.O. and WHITE, A.M., 1997, Studies on transparent exopolymers particles (TEP) produced in the Ross Sea (Antarctica) and by *Phaeocystis Antarctica* (Prymnesiophyceae). *Journal of Phycology*, **33**, pp. 368–376.

JERLOV, N.G., 1976, *Optical Oceanography* (New York: Elsevier).

LEE, Z.P., CARDER, K. and ARNONE, R.A., 2002, Deriving inherent optical properties from water color: a multiband quai-analytical algorithm for optically deep waters. *Applied Optics*, **41**, pp. 5755–5772.

LEE, Z., CARDER, K., HAWES, S.K., STEWARD, R.G., PEACOCK, T.G. and DAVIS, C.O., 1994, Model for interpretation of hyperspectral remote-sensing reflectance. *Applied Optics*, **33**, pp. 5721–5731.

LEE, Z.P., CARDER, K., MARRA, J., STEWARD, R.G. and PERRY, M.J., 1996, Estimating primary production at depth from remote sensing. *Applied Optics*, **35**, pp. 463–474.

LEE, Z.P., CARDER, K., MOBLEY, C., STEWARD, R.G. and PATCH, J., 1999, Hyperspectral remote sensing for shallow waters: 2. Deriving bottom depths and water properties by optimization. *Applied Optics*, **38**, pp. 3831–3843.

MITCHELL, B.G. and HOLM-HANSEN, O., 1991, Bio-optical properties of Antarctic Peninsula waters: differentiation from temperate ocean models. *Deep-Sea Research*, **38**, pp. 1009–1028.

MOBLEY, C.D., 1994, Light and Water: Radiative Transfer in Natural Waters (San Diego, CA: Academic Press).

MOLINE, M.A., ARNONE, R., BERGMANN, T., GLENN, S., OLIVER, M.J., ORRICO, C., SCHOFIELD, O. and TOZZI, S., 2004b, Variability in spectral backscatter estimated from satellite and its relation to in situ measurements in optically complex coastal waters. *International Journal of Remote Sensing*, **25**, pp. 1465–1468.

MOLINE, M.A., CLAUSTRE, H., FRAZER, T.K., SCHOFIELD, O. and VERNET, M., 2004a, Alteration of the food web along the Antarctic Peninsula in response to a regional warming trend. *Global Change Biology*, **10**, pp. 1973–1980.

MONTES-HUGO, M.A., 2005, Monte Carlo simulations as a tool to optimize target detection by AUV/ROV laser line scanners. Masters thesis, University of South Florida.

MOREL, A., 1973, Diffussion de la lumière per les eaux de mer: Résultats experimentaux et approach théoretique. *Agard Lecture Series*, **61**, pp. 3.1.1–3.1.7.6.

MOREL, A., 1974, Optical properties of pure waterand pure sea water. In *Optical Aspects of Oceanography*, N.G. Jerlov and E.S. Nielsen (Eds), pp. 1–24 (London: Academic Press).

MOREL, A., 1991, Light and marine photosynthesis: a spectral model with geochemical and climatological implications. *Progress in Oceanography*, **26**, pp. 263.

NECKEL, H. and LABS, D., 1984, The solar radiation between 3300 and 12500. *A Solar Physics*, **90**, pp. 205–258.

OISHI, T., 1990, Significant relationship between the backward scattering coefficient of sea water and the scatterance at 120°. *Applied Optics*, **29**, pp. 4658–4665.

O'REILLY, J.E., MARITORENA, S., MITCHELL, B.G., SIEGEL, D.A., CARDER, K.L., GARVER, S.A., KARHU, M., GARVER, S.A. and MCCLAIN, S.A., 1998, Ocean color algorithms for SeaWiFS. *Journal of Geophysical Research*, **103**, pp. 24937–24953.

PEGAU, W.S., GRAY, D. and ZANAVELD, J.R.V., 1997, Absorption and attenuation of visible and near-infrared light in water: Dependence on temperature and salinity. *Applied Optics*, **36**, pp. 6035–6046.

PEGAU, W.S. and ZANAVELD, J.R., 1993, Temperature-dependent absorption of water in the red and near-infrared portions of the spectrum. *Limnology and Oceanography*, **38**, pp. 188–192.

POPE, R.M. and FRY, E.S., 1997, Absorption spectrum (380–700 nm) of pure water, II. Integrating cavity measurements. *Applied Optics*, **36**, pp. 8710–8723.

QUIRANTES, A. and BERNARD, S., 2004, Light scattering by marine algae: two-layer spherical and nonspherical models. *Journal of Quantitative Spectroscopy and Radiative Transfer*, **89**, pp. 311–321.

REYNOLDS, R.A., STRAMSKI, D. and MITCHELL, B.G., 2001, A chlorophyll-dependent semianalytical reflectance model derived from field measurements of absorption and backscattering coefficients within the Southern Ocean. *Journal of Geophysical Research*, **106**, pp. 7125–7138.

RODRIGUEZ, F., VARELA, M. and ZAPATA, M., 2002, Phytoplankton assemblages in the Gerlache and Bransfield Straits (Antarctic Peninsula) determined by light microscopy and CHEMTAX analysis of HPLC pigment data. *Deep-Sea Research II*, **49**, pp. 723–747.

SMETACEK, V., KLAAS, C., MENDEN-DEUER, S. and RYNEARSON, T.A., 2002, Mesoscale distribution of dominant diatom species relative to the hydrological field along the Antarctic Polar Front. *Deep-Sea Research II*, **49**, pp. 3835–3848.

SMETACEK, V., SCHAREK, R. and NÖTHIG, E.M., 1990, Seasonal and regional variation in the pelagial and its relationship to the life history cycle of Krill. In *Antarctic Ecosystems, Ecological Change and Conservation*, K.R. Kerry and G. Hempel (Eds), pp. 103–114 (Heidelberg, Germany: Springer).

SMITH, R.C. and BAKER, K.S., 1981, Optical properties of the clearest natural waters (200–800 nm). *Applied Optics*, **20**, pp. 177–184.

SMITH, R.C. and BAKER, K., 1986, Analysis of ocean optical data II. *Proceedings of SPIE—The International Society for Optical Engineering*, **637**, pp. 95–107.

SMITH, R.C., BAKER, K.S. and DUSTAN, P., 1981, Fluorometric techniques for the measurement of oceanic chlorophyll in the support of remote sensing. Technical Report, Scripps Institution of Oceanography, University of California, San Diego (Ref. 81–17).

SMITH, R.C., BAKER, K.S., FRASER, W.R., HOFMANN, E.E., KARL, D.M., KLINCK, J.M., QUETIN, L.B., PREZELIN, B.B., ROSS, R.M. and TRIVELPIECE, W.Z., 1995, The Palmer-LTER: A long-term ecological research program at Palmer Station, Antarctica. *Oceanography*, **8**, pp. 77–86.

SMITH, W.O. JR. and SAKSHAUG, E., 1990, Polar phytoplankton. In *Polar Oceanography, Part B. Chemistry, Biology, and Geology*, W.O. Smith Jr (Ed.), pp. 477–525 (London: Academic Press).

SMITH, R.C., MENZIES, D.W. and BOOTH, C.R., 1997, Oceanographic biooptical profiling system II. *Proceedings of SPIE—The International Society for Optical Engineering*, **2963**, pp. 777–786.

SMITH, R. and STAMMERJOHN, S.E., 2001, Variations of surface air temperature and sea ice extent in the western Antarctic Peninsula region. *Annals of Glaciology*, **33**, pp. 493–500.

STRAMSKI, D., BOSS, E., BOGUCKI, D. and VOSS, K.J., 2004, The role of seawater constituents in light backscattering in the ocean. *Progress in Oceanography*, **61**, pp. 27–56.

STRAMSKI, D., BRICAUD, A. and MOREL, A., 2001, Modeling the inherent optical of the ocean based on the detail composition of the planktonic community. *Applied Optics*, **40**, pp. 2929–2945.

STRAMSKI, D. and WOZNIAK, S.B., 2005, On the role of colloidal particles in light scattering in the ocean. *Limnology and Oceanography*, **50**, pp. 1581–1591.

TOOLE, D.A., SIEGEL, D.A., MENZIES, D.W., NEUMANN, M.J. and SMITH, R.C., 2000, Remote-sensing reflectance determinations in the coastal ocean environment: impact of instrumental characteristics and environmental variability. *Applied Optics*, **39**, pp. 456–468.

TREMBLAY, J.E. and LEGENDRE, L., 1994, A model for the size-fractioned biomass and production of marine phytoplankton. *Limnology and Oceanography*, **39**, pp. 2004–2014.

TREMBLAY, J.E., LUCAS, M.I., KATTNER, G., POLLARD, R., STRASS, V.H., BATHMANN, U. and BRACHER, A., 2002, Significance of the Polar Frontal Zone for large-sized diatoms and new production during summer in the Atlantic sector of the Southern Ocean. *Deep-Sea Research II*, **49**, pp. 3793–3811.

TWARDOWSKI, M.S., BOSS, E., SULLIVAN, J.M. and DONAGHAY, P.L., 2004, Modeling the spectral shape of absorption by chromophoric dissolved organic matter. *Marine Chemistry*, **89**, pp. 69–88.

VAILLANCOURT, R.D., BROWN, C.W., GUILLARD, R.R.L. and BALCH, W.M., 2004, Light backscattering properties of marine phytoplankton: relationships to cell size, chemical composition and taxonomy. *Journal of Plankton Research*, **26**, pp. 191–212.

VAN DE HULST H.C., 1957, *Light Scattering by Small Particles* (Chichester, UK: Wiley).

VIDUSSI, F., CLAUSTRE, H., MANCA, B.B., LUCHETTA, A. and MARTY, J.C., 2001, Phytoplankton pigment distribution in relation to upper thermocline circulation in the eastern Mediterranean Sea during winter. *Journal of Geophysical Research*, **106**, pp. 19,939–19,956.

WALSH, J.J., DIETERLE, D.A. and LENES, J., 2001, A numerical analysis of carbon dynamics of the Southern Ocean phytoplankton community: the roles of light and grazing in effecting both sequestration of atmospheric CO_2 and food availability to larval krill. *Deep-Sea Research Part I*, **48**, pp. 1–48.

WEIDEMANN, A.D., STAVN, R.H., ZANAVELD, J.R.V. and WILCOX, M.R., 1995, Error in predicting hydrosol backscattering from remotely sensed reflectance. *Journal of Geophysical Research*, **100**, pp. 13,163–13,177.